Paleolatitudes of the Tibetan Himalaya from primary and secondary magnetizations of Jurassic to Lower Cretaceous sedimentary rocks

Wentao Huang, Douwe J.J. van Hinsbergen, Mark J. Dekkers, Eduardo Garzanti, Guillaume Dupont-Nivet, Peter C. Lippert, Xiaochun Li, Marco Maffione, Cor G. Langereis, Xiumian Hu, et al.

RESEARCH ARTICLE

Key Points:
- Low Cretaceous volcaniclastic sandstones retain a primary remanence
- Jurassic limestones were chemically remagnetized
- Tibetan Himalaya was part of India plate in Early Cretaceous

Supporting Information:
- Supporting Information

Correspondence to:
W. Huang,
W.Huang@uu.nl

Paleolatitudes of the Tibetan Himalaya from primary and secondary magnetizations of Jurassic to Lower Cretaceous sedimentary rocks

Wentao Huang[1,2], Douwe J. J. van Hinsbergen[2], Mark J. Dekkers[2], Eduardo Garzanti[3], Guillaume Dupont-Nivet[1,2,4,5], Peter C. Lippert[6,7], Xiaochun Li[8], Marco Maffione[2], Cor G. Langereis[2], Xiumian Hu[9], Zhaojie Guo[1], and Paul Kapp[6]

[1]Key Laboratory of Orogenic Belts and Crustal Evolution, Ministry of Education, School of Earth and Space Sciences, Peking University, Beijing, China, [2]Department of Earth Sciences, Utrecht University, Utrecht, Netherlands, [3]Department of Earth and Environmental Sciences, University of Milano-Bicocca, Milano, Italy, [4]Géosciences Rennes, UMR 6118, Université de Rennes 1, Rennes, France, [5]Institute of Earth and Environmental Science, University of Potsdam, Potsdam, Germany, [6]Department of Geosciences, University of Arizona, Tucson, Arizona, USA, [7]Department of Geology and Geophysics, University of Utah, Salt Lake City, Utah, USA, [8]Department of Earth Sciences, University of Hong Kong, Hong Kong, China, [9]State Key Laboratory of Mineral Deposit Research, School of Earth Sciences and Engineering, Nanjing University, Nanjing, China

Abstract The Tibetan Himalaya represents the northernmost continental unit of the Indian plate that collided with Asia in the Cenozoic. Paleomagnetic studies on the Tibetan Himalaya can help constrain the dimension and paleogeography of "Greater India," the Indian plate lithosphere that subducted and underthrusted below Asia after initial collision. Here we present a paleomagnetic investigation of a Jurassic (limestones) and Lower Cretaceous (volcaniclastic sandstones) section of the Tibetan Himalaya. The limestones yielded positive fold test, showing a prefolding origin of the isolated remanent magnetizations. Detailed paleomagnetic analyses, rock magnetic tests, end-member modeling of acquisition curves of isothermal remanent magnetization, and petrographic investigation reveal that the magnetic carrier of the Jurassic limestones is authigenic magnetite, whereas the dominant magnetic carrier of the Lower Cretaceous volcaniclastic sandstones is detrital magnetite. Our observations lead us to conclude that the Jurassic limestones record a prefolding remagnetization, whereas the Lower Cretaceous volcaniclastic sandstones retain a primary remanence. The volcaniclastic sandstones yield an Early Cretaceous paleolatitude of 55.5°S [52.5°S, 58.6°S] for the Tibetan Himalaya, suggesting it was part of the Indian continent at that time. The size of "Greater India" during Jurassic time cannot be estimated from these limestones. Instead, a paleolatitude of the Tibetan Himalaya of 23.8°S [21.8°S, 26.1°S] during the remagnetization process is suggested. It is likely that the remagnetization, caused by the oxidation of early diagenetic pyrite to magnetite, was induced during 103–83 or 77–67 Ma. The inferred paleolatitudes at these two time intervals imply very different tectonic consequences for the Tibetan Himalaya.

1. Introduction

Paleogeographic reconstructions of intensely deformed terranes in the India-Asia collision zone can be quantified by using paleomagnetic data to constrain vertical axis rotations and, importantly, paleolatitude. There is an ongoing debate on the paleolatitude history of the Tibetan Himalaya, which represents the northernmost continental unit of the Indian plate that first collided with Asia [*Gansser*, 1964; *Sciunnach and Garzanti*, 2012]. Paleomagnetic data from uppermost Cretaceous and Paleogene rocks from the Tibetan Himalayan show a paleolatitudinal separation from India of 24.1 ± 6.3° (2675 ± 699 km N-S) [*Patzelt et al.*, 1996; *Dupont-Nivet et al.*, 2010a; *Yi et al.*, 2011; *van Hinsbergen et al.*, 2012], which, when combined with paleolatitude results from the Lhasa terrane of the Asian margin, suggests the Tibetan Himalaya-Lhasa collision occurred by ~50 Ma if not several million years earlier [*Dupont-Nivet et al.*, 2010b; *van Hinsbergen et al.*, 2012; *Lippert et al.*, 2014]. Paleomagnetic data from the Lower Cretaceous of the Tibetan Himalaya [*Klootwijk and Bingham*, 1980], however, show an insignificant paleolatitudinal separation from India, which led *van Hinsbergen et al.* [2012] to conclude that the Tibetan Himalaya must have rifted and drifted away from India during the Cretaceous, a view that has since been widely debated [*Aitchison and Ali*, 2012; *DeCelles et al.*,

2014; *Garzanti and Hu*, 2014; *Wang et al.*, 2014]. Inspired by this problem concerning the kinematic evolution of the passive northern Indian margin and the extent of "Greater India" before the India-Asia collision, we investigate in this paper Jurassic (limestones) to Lower Cretaceous (volcaniclastic sandstones) sedimentary rocks of the Tibetan Himalaya near the village of Wölong, which were well described and dated by *Jadoul et al.* [1998].

A substantial challenge to studying the paleomagnetism of the Tibetan Himalayan sedimentary rocks is that remagnetization is pervasive; natural remanent magnetizations (NRM) with a primary origin are rarely found in these units [*Appel et al.*, 2012]. Only a few Triassic and Upper Cretaceous to Paleogene units with a primary remanence have been reported [*Klootwijk and Bingham*, 1980; *Klootwijk et al.*, 1983; *Besse et al.*, 1984; *Appel et al.*, 1991; *Patzelt et al.*, 1996; *Appel et al.*, 1998; *Schill et al.*, 2002; *Crouzet et al.*, 2003; *Yi et al.*, 2011; *Ran et al.*, 2012]. Thus, the onus for any paleomagnetic study of these units is to thoroughly evaluate the origin and timing of the characteristic magnetization. Here we use petrographic, geochemical, and rock magnetic studies to identify mineralogical changes that are diagnostic of remagnetization [*Roberts and Weaver*, 2005; *Dekkers*, 2012; *Elmore et al.*, 2012; *Jackson and Swanson-Hysell*, 2012]. Given the widespread reporting of remagnetization of Tibetan Himalaya sedimentary rocks, we completed the following analyses. (1) We isolated paleomagnetic directions from the limestones and volcaniclastic rocks of the section using thermal and alternating field (AF) demagnetizations. (2) We apply a fold test to constrain the time of the remanence acquisition relative to contractional deformation. (3) We provided detailed rock magnetic analyses, utilizing thermomagnetic experiments, hysteresis measurements, first-order reversal curve (FORC) diagrams, and isothermal remanent magnetization (IRM) component analysis to investigate the carriers of the remanent magnetization(s). (4) We apply end-member modeling of IRM-acquisition curves [*Gong et al.*, 2009] to identify potential mechanisms for the acquisition of remanent magnetization. (5) Finally, we use scanning electron microscopy (SEM) and energy-dispersive X-ray spectrometry (EDS) to visually characterize the magnetic minerals and verify rock magnetic results. With this information, we evaluate whether or not the NRMs obtained from the Jurassic limestones and Lower Cretaceous volcaniclastic sandstones are primary. Acquisition mechanisms and ages of the remanent magnetizations carried by the Jurassic limestones and Lower Cretaceous volcaniclastic sandstones are discussed, and we evaluate the implications for the paleolatitudinal separation of the Tibetan Himalaya with respect to cratonic India.

2. Geological Background

The Mesozoic Tibetan Himalaya sedimentary successions were deposited on the northern passive margin of the Indian subcontinent (Figure 1a). The section studied here (28.47889°N, 87.03528°E, elevation 4348 m) is located near the village of Wölong on the road to the Everest Base Camp and is 20 km southwest of Tingri in southern Tibet (Figure 1a). Jurassic to Lower Cretaceous sedimentary successions are folded into a syncline with an overturned northern limb (Figure 1b) [*Jadoul et al.*, 1998]. Detailed stratigraphic descriptions of the section can be found in supporting information Text S1.

Exposed in the lower part of the section is the ~200 m thick, middle Lower Jurassic to lower Middle Jurassic Kioto Group of platform limestones. Two units (K_1 and K_2) were informally distinguished (Figure 1b) [*Jadoul et al.*, 1998]. The overlying Laptal Formation is 42–45 m thick and is mainly composed of late Bajocian marly siltstones in the lower part and Bathonian subtidal limestones in the upper part. The ≤10 m thick Ferruginous Oolite Formation (FOF) above was deposited during the late Bathonian to middle Callovian [*Garzanti et al.*, 1989]. It mainly consists of oo-bioclastic rudstones and minor feldspato-quartzose detritus. The Dangar Formation with a thickness of ≤60 m is comprising gray marly limestones. Feldspato-quartzose silt occurs in the upper part. Calcareous nannofossils indicate a Callovian to Oxfordian age. The overlying 18–20 m of black shales with limestone nodules, and with calcareous silty layers intercalated in the upper part, are ascribed to the Spiti Shale. Calcareous nannofossils indicate an age not younger than the Oxfordian.

The Spiti Shale transitions gradually upward to the >400 m thick Wölong Formation (Figure 1b), which is mainly composed of siltstones and volcaniclastic sandstones intercalated with black shales. The lithostratigraphy and detrital zircon geochronology of the Wölong volcaniclastic sandstones have been described at the Gucuo locality near Old Tingri in southern Tibet [*Hu et al.*, 2010]. There the Wölong volcaniclastic rocks have a maximum allowable deposition age of ~120 Ma. At this locality, the volcaniclastic sandstones are separated from underlying Upper Tithonian strata by a fault and are conformably covered by Upper Albian strata [*Hu et al.*, 2010]. The other reported Lower Cretaceous volcaniclastic rocks of the Tibetan Himalaya is located in the Babazhadong area, where volcaniclastic sandstones of the Rilang Formation overlies Jurassic strata conformably and have a
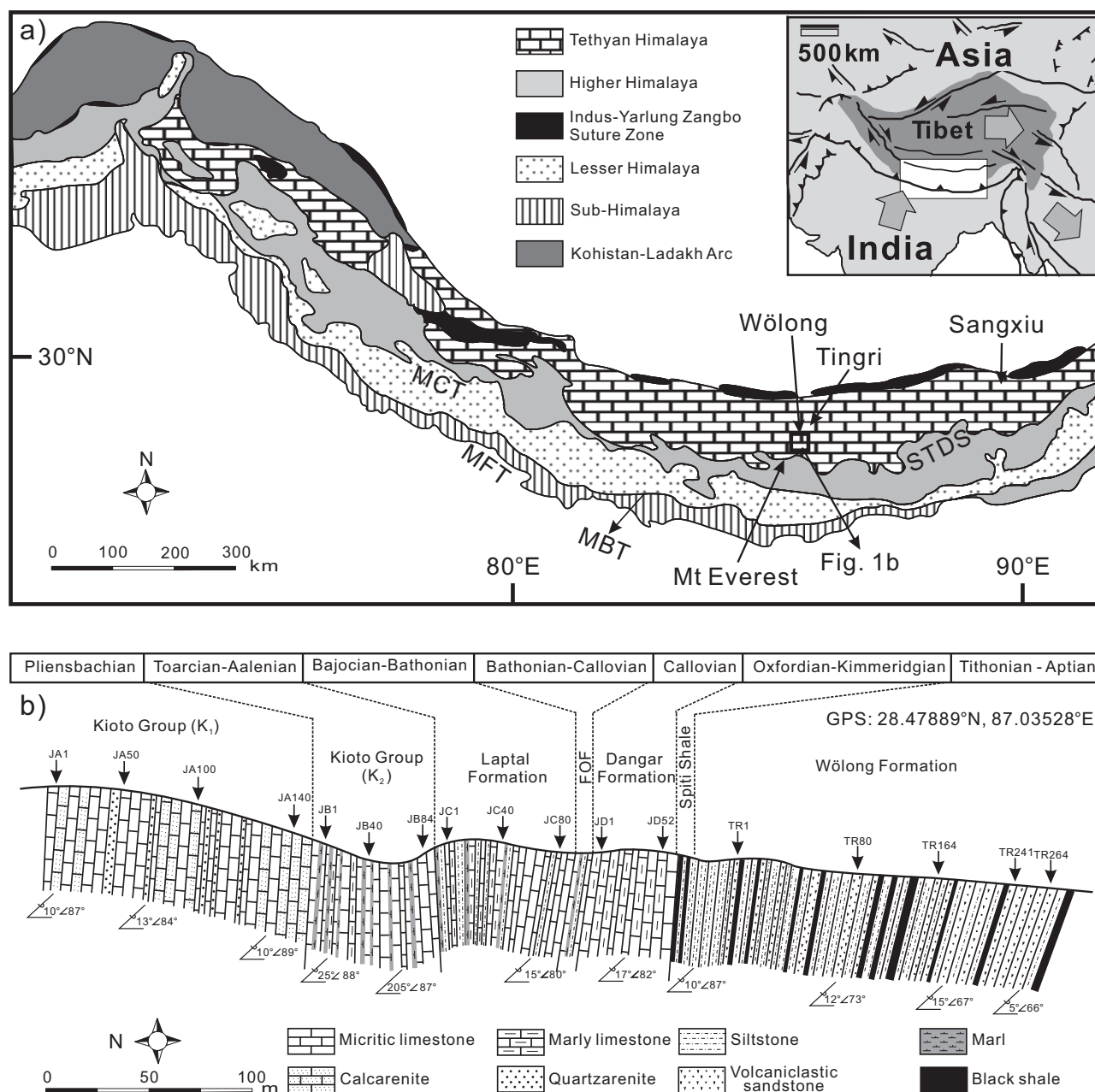
Figure 1. (a) Simplified geological map of the Himalayas, modified from *Gansser* [1964] and *Hu et al.* [2010]. MFT: Main Frontal Thrust; MBT: Main Boundary Thrust; MCT: Main Central Thrust; and STDS: South Tibetan Detachment System. (b) Profile of the sampled section.

maximum depositional age of ∼134 Ma [*Du et al.*, 2015]. The Wölong Formation in this study overlies the Kimmerdgian to Tithonian Spiti Shale conformably. We therefore infer that the deposition of the Wölong Formation in our study is probably older than that at the Gucuo locality [*Hu et al.*, 2010], but similar to the volcaniclastic rocks in the Babazhadong area [*Du et al.*, 2015] with a maximum depositional age of 134 ± 4 Ma.

3. Paleomagnetic Sampling

Typical paleomagnetic cores with a diameter of 2.5 cm were collected using a portable gasoline-powered drill and were oriented with magnetic and sun compasses. We collected 624 individual paleomagnetic cores from all the units of the Jurassic to Lower Cretaceous successions from the northern overturned limb of the syncline (Figure 1b). One hundred forty oriented cores (JA1–JA140, sample code progressing up section) are from unit K_1, 84 cores (JB1–JB84) are from unit K_2, 80 cores (JC1–JC80) are from the Laptal Formation, 52

cores (JD1–JD52) are from the Dangar Formation, and 264 cores (TR1–TR264) are from the volcaniclastic sandstones of the Wölong Formation. Twenty-seven limestone cores were also collected from unit K_2 exposed in the southern limb of the syncline to allow for a fold test. Bedding attitudes determined from the planar orientation of the sedimentary layers were measured throughout the section at each sampling location for the tilt correction (Figure 1b).

4. Paleomagnetism

4.1. Demagnetization

Characteristic remanent magnetization (ChRM) directions were isolated using both alternating field (AF) and thermal demagnetization. AF demagnetization was applied to all the specimens from all cores with an in-house developed robotized sample handler [*Mullender et al.*, 2005] attached to a horizontal pass-through 2G Enterprises DC SQUID magnetometer (noise level $1-2 \times 10^{-12}$ Am^2) hosted in the magnetically shielded room (residual field <200 nT) at the Fort Hoofddijk Paleomagnetic Laboratory, Utrecht University (Netherlands). Specimens were progressively demagnetized by successive AF steps of 5, 10, 15, 20, 25, 30, 35, 40, 45, 50, 55, 60, 65, 70, 80, 90, and 100 mT. In addition, 120 specimens selected throughout the collection were treated by thermal demagnetization. These specimens were heated and cooled in a magnetically shielded ASC oven (Model TD48-SC) that has a residual field <10 nT. Their NRM was measured on a horizontal 2G Enterprises DC SQUID magnetometer (noise level 3×10^{-12} Am^2). Specimens were progressively demagnetized by successive temperature steps at 100, 140, 180, 210, 240, 270, 300, 330, 360, 390, 420, 450, 480, 510, 530, 550, 570, and 585°C until complete demagnetization of the NRM.

For the Jurassic limestones, an NRM component was usually removed at a low field level (20 mT) or low temperature (210°C) by AF and thermal treatments (Figures 2a–2i), respectively. After removing this weak component, a second component was often isolated by 20–80 mT and 240–510°C (Figures 2a–2i). Most volcaniclastic specimens from the Lower Cretaceous Wölong Formation also reveal two components. The first component was commonly removed below 20 mT or 200°C (Figures 2j–2p). The second component could usually be isolated between 20 and 70 mT or 200 and 530°C or 200 and 570°C. Magnetic intensity of some specimens increased after heating up to and beyond 530°C (Figure 2j).

4.2. ChRM Directions

Principal component analysis [*Kirschvink*, 1980] on at least five successive steps resulted in precisely determined ChRM directions for most specimens. Some specimens yielding NRM directions between two overlapping coercivity or temperature components were also analyzed using the great circle approach [*McFadden and McElhinny*, 1988]. AF and thermal demagnetization paths for specimens from the same sample are generally comparable (Figures 2a, 2d, 2h, and 2j). Considering that thermal demagnetization results were sometimes more erratic and yielded higher maximum angular deviation (MAD) values than the AF treatment, we calculated most of the ChRM directions from the AF demagnetization results. Directions with MAD values $>15°$ were systematically rejected from further analysis (supporting information Table S1).

We isolated the low-coercivity/low-temperature direction in 301 of 624 individual specimens. After excluding directions which fall $>45°$ from the mean direction, we calculated a mean direction of $D_g = 359.5°$, $I_g = 38.9°$ (n = 238, K = 10.5, $A_{95} = 3°$; "g" stands for geographic coordinates) (Figure 3d). The isolated ChRMs from all units of the Jurassic limestones are of normal polarity (Figures 3a–3d). We binned the results into the stratigraphic intervals identified in the geological setting.

The mean ChRM direction of the specimens from unit K_1 that pass our data selection criteria is $D_s \pm \Delta D_s = 331.2 \pm 3.6°$, $I_s \pm \Delta I_s = -41.1 \pm 4.5°$ (n = 112, K = 17.1, $A_{95} = 3.3°$, "s" referring to stratigraphic coordinates) (Figure 3a). The mean ChRM direction of the specimens from unit K_2 that pass our data selection criteria is $D_s \pm \Delta D_s = 334.6 \pm 3.1°$, $I_s \pm \Delta I_s = -42.2 \pm 3.7°$ (n = 83, K = 31.6, $A_{95} = 2.8°$) (Figure 3b and supporting information Table S2). Stable ChRM directions could be determined only from a small number of specimens in the Laptal Formation (Figure 3c). The mean ChRM direction of the specimens from the Laptal Formation that pass our data selection criteria is $D_s \pm \Delta D_s = 338.9 \pm 6.8°$, $I_s \pm \Delta I_s = -40.2 \pm 8.7°$ (n = 45, K = 12.4, $A_{95} = 6.3°$) (Figure 3c and supporting information Table S1). Most specimens from the Dangar Formation record only one component, which is similar to the low-coercivity/low-temperature component observed in other specimens (Figure 3d). A ChRM direction could be isolated from just a single specimen.
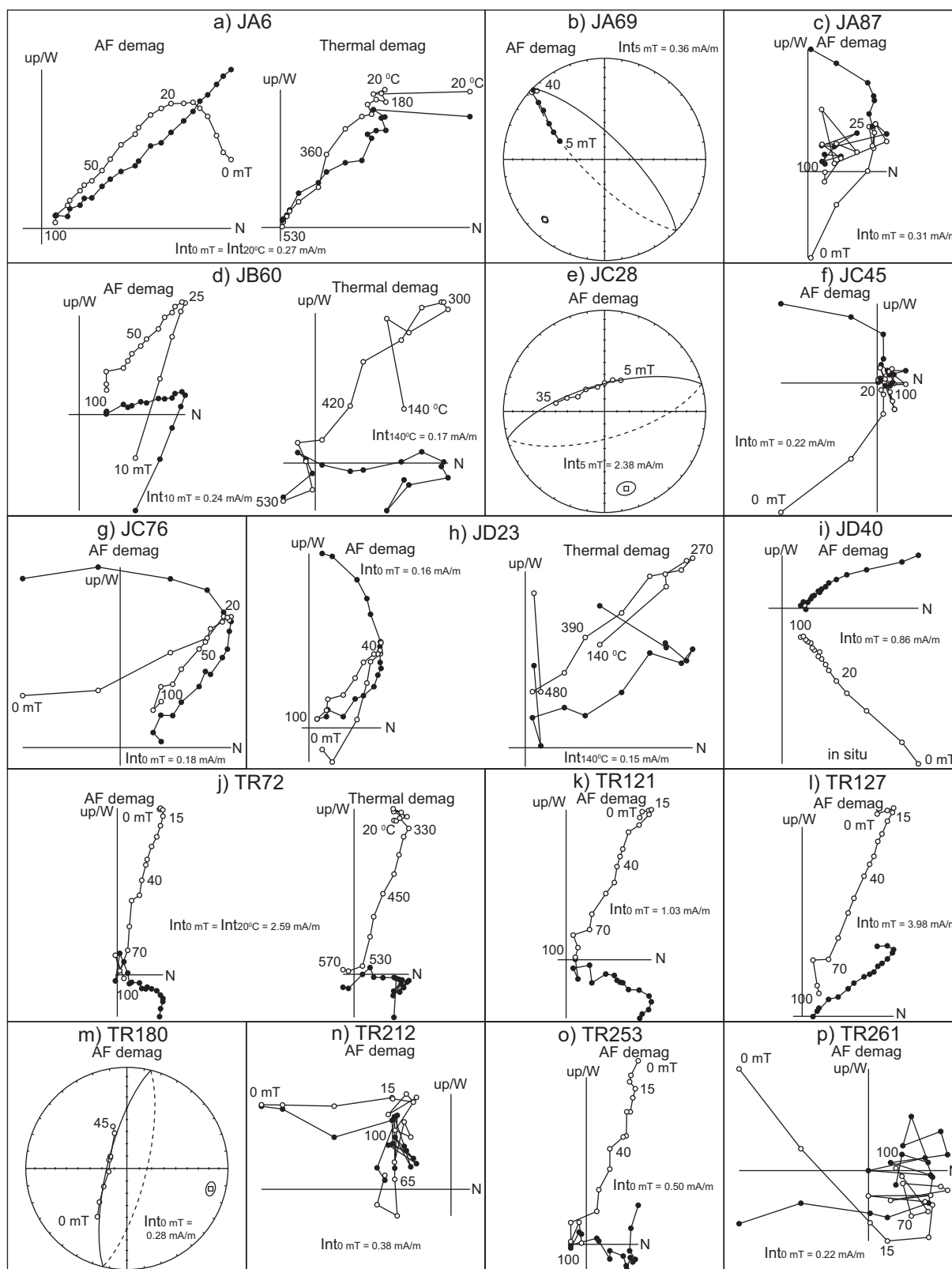
Figure 2. Representative demagnetization diagrams for samples covering the sampled sections from Jurassic limestones to Lower Cretaceous volcaniclastic sandstones. All diagrams are displayed after bedding tilt correction except for Figure 2i, which is displayed before tilt correction. Closed (open) symbols represent the projection of vector endpoints on the horizontal (vertical) plane; values represent the alternating field and thermal demagnetization steps in mT and °C, respectively.

a) K₁

n=64		n=112
D=221°		D=331.2°
I=-31.1°		I=-41.1°
K=20.2		K=17.1
A95=4		A95=3.3
	n=64	Stratigraphic
Geographic	D=329.9°	
	I=-40.6°	
	K=18.9	
	A95=4.2 Stratigraphic	

b) K₂

n=78		
D=239.4°		
I=-31.3°		
K=26.1		n=83
A95=3.2		D=334.6°
Geographic	n=80	I=-42.2°
	D=334.7°	K=31.6
	I=-42.4°	A95=2.8
	K=30.8 Stratigraphic	Stratigraphic
	A95=2.9	

c) Laptal Formation

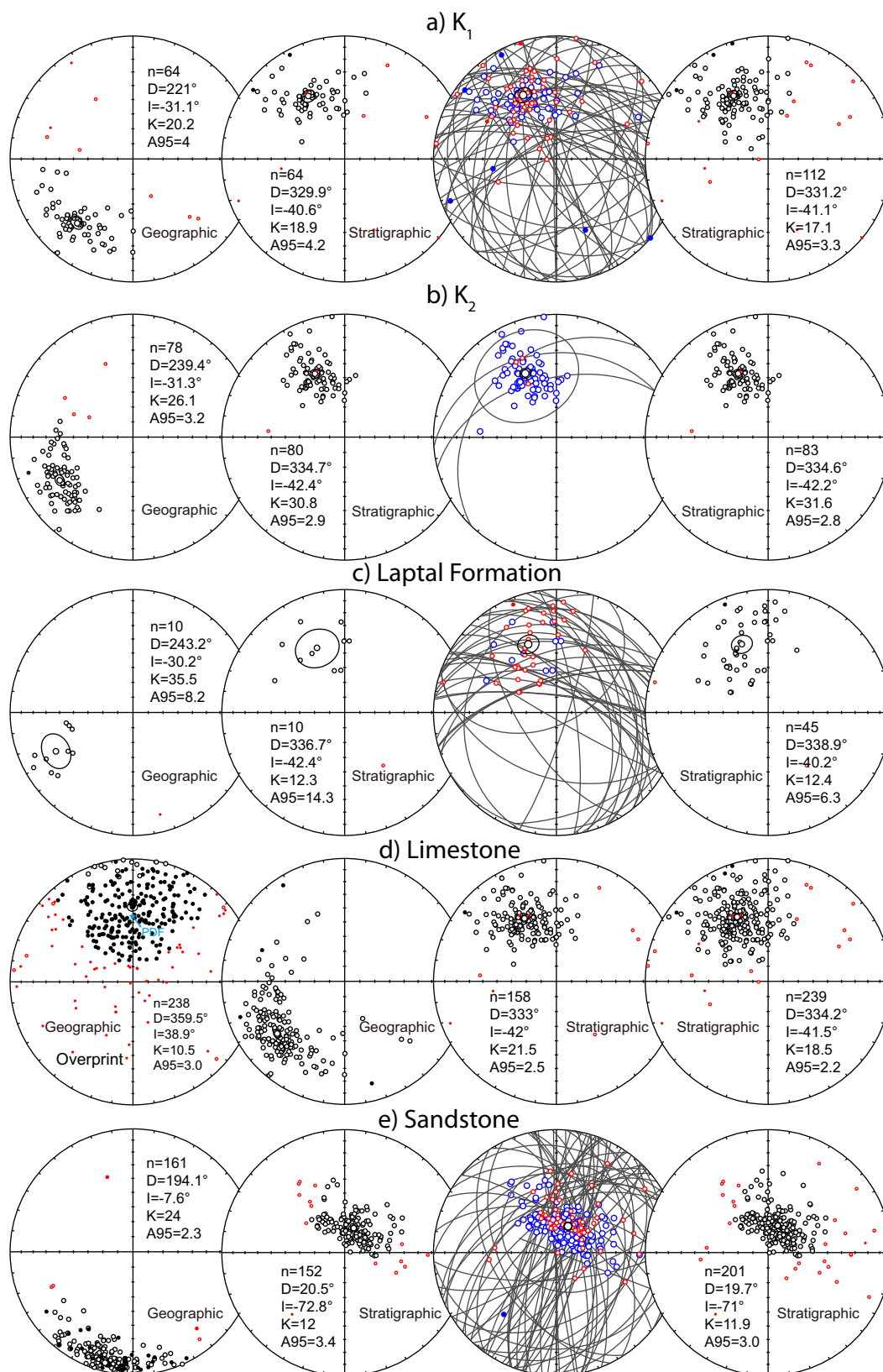|		
n=10		
D=243.2°		
I=-30.2°		
K=35.5		n=45
A95=8.2		D=338.9°
Geographic	n=10	I=-40.2°
	D=336.7°	K=12.4
	I=-42.4°	A95=6.3
	K=12.3 Stratigraphic	Stratigraphic
	A95=14.3	

d) Limestone

		n=239
Geographic		D=334.2°
	n=238	I=-41.5°
Overprint	D=359.5°	K=18.5
	I=38.9°	A95=2.2
	K=10.5 Geographic	Stratigraphic
	A95=3.0	
	n=158 Stratigraphic	
	D=333°	
	I=-42°	
	K=21.5	
	A95=2.5	

e) Sandstone

n=161		
D=194.1°		
I=-7.6°		
K=24		n=201
A95=2.3		D=19.7°
Geographic	n=152	I=-71°
	D=20.5°	K=11.9
	I=-72.8°	A95=3.0
	K=12 Stratigraphic	Stratigraphic
	A95=3.4	

Figure 3.

This ChRM direction is similar to those isolated from specimens in units K_1, K_2, and the Laptal Formation (supporting information Table S1).

The common true mean direction (CTMD) test shows that the mean ChRM directions isolated from specimens in units K_1, K_2, and the Laptal Formation are indistinguishable from each other [*McFadden and Lowes*, 1981]. Therefore, we combined all the results from specimens from the Jurassic limestones in these four units. The mean ChRM direction defined by principal component analysis is $D_s \pm \Delta D_s = 333.0 \pm 2.7°$, $I_s \pm \Delta I_s = -42.0 \pm 3.3°$ ($n = 158$, $K = 21.5$, $A_{95} = 2.5°$) (Figure 3d and supporting information Table S1). The mean direction calculated from both principal component analysis and great circle analysis is $D_s \pm \Delta D_s = 334.2 \pm 2.4°$, $I_s \pm \Delta I_s = -41.5 \pm 2.9°$ ($n = 239$, $K = 18.5$, $A_{95} = 2.2°$) (Figure 3d and supporting information Table S1). We evaluate the possibility of inclination shallowing in the Jurassic limestones by applying the elongation/inclination correction method [*Tauxe and Kent*, 2004] to the ChRM directions defined by principal component analysis. The mean inclination was "restored" from $-42.0 \pm 3.3°$ to $-43.2°$ $[-52.0°, -40.8°]$, suggesting that the limestones do not suffer from inclination shallowing. This result is similar to observations from other marine carbonate successions in the region [*van Hinsbergen et al.*, 2012].

ChRM directions were also isolated from the 27 limestone specimens collected in the southern limb of the syncline. The mean direction from this locality is $D_s \pm \Delta D_s = 326.8 \pm 8.5°$, $I_s \pm \Delta I_s = -49.5 \pm 8.3°$ ($n = 27$, $K = 15.3$, $A_{95} = 7.4°$). These results allow us to apply a fold test to the Jurassic limestones to assess whether the interpreted ChRM has a prefolding origin. Before tilt correction, the ChRM directions of limestone specimens from the two limbs of the syncline are very distinct from each other (Figure 4a). After tilt correction, however, the ChRM directions of limestone specimens from the two limbs are similar (Figure 4a). The nonparametric fold test of *Tauxe and Watson* [1994] is positive with best grouping reached at 91–95% untilting (Figure 4b). This fold test shows that the magnetization of the isolated ChRM directions recovered from the Jurassic limestones was largely acquired before folding.

Most volcaniclastic specimens record directions that decay linearly toward the origin, although some specimens have erratic demagnetization trajectories (Figure 3e). The mean ChRM direction defined by principal component analysis is $D_s \pm \Delta D_s = 20.5 \pm 6.6°$, $I_s \pm \Delta I_s = -72.8 \pm 2.2°$ ($n = 152$, $K = 12$, $A_{95} = 3.4°$) (Figure 3e). The mean direction with the results from great circle analysis is $D_s \pm \Delta D_s = 19.7 \pm 5.3°$, $I_s \pm \Delta I_s = -71 \pm 2°$ ($n = 201$, $K = 11.9$, $A_{95} = 3°$) (Figure 3e and supporting information Table S1). We can apply neither a fold test nor a reversals test to the volcaniclastic rocks because there are no suitable outcrops for paleomagnetic sampling of the equivalent rocks from the southern limb of the syncline and because the directions are exclusively of normal polarity. The mean ChRM A_{95} (3.4°) falls within the reliability envelope of *Deenen et al.* [2011] (for $n = 152$, $A_{95(min)} = 1.6°$, $A_{95(max)} = 3.5°$); this shows that the measured scatter can be straightforwardly explained by and likely represents paleosecular variation of the geomagnetic field. To assess the potential shallow bias of the magnetic inclination, we applied the elongation/inclination correction procedure to the volcaniclastic rocks [*Tauxe and Kent*, 2004]. The expected line defined by the expected inclination-elongation pairs according to *Tauxe* [2005] does not intersect with the bootstrapped data sets, indicating that the volcaniclastic rocks are not flattened; therefore, no inclination correction is applied to the volcaniclastic sandstones.

5. Rock Magnetism

5.1. Thermomagnetic Runs

Twenty-eight representative samples from all stratigraphic units of the section (7 from unit K_1, 5 from unit K_2, 3 from the Laptal Formation, 3 from the Dangar Formation, and 10 from the Wölong Formation) were subjected to high-field thermomagnetic experiments following the procedure described in *Huang et al.* [2013]. The successive heating and cooling steps are 150, 100, 250, 150, 400, 300, 520, 420, 620, 500, 700, and 20°C.

Figure 3. (a) Equal-area projections of the isolated ChRM directions from K_1 limestones. Red dots (circles) are rejected by the 45° cut off criterion [*Deenen et al.*, 2011]. Blue dots (circles) are the results calculated by great circle analysis. Large circles represent the mean ChRM directions and 95% confidence limit. From left to right: ChRM directions acquired by line fit in geographic coordinates; ChRM directions acquired by line fits in stratigraphic coordinates; result of the great circle analysis; ChRM directions acquired by both line fits and great circle analysis. (b and c) Same equal-area projections of the isolated ChRM directions from unit K_2 and Laptal limestones, respectively. (d) From left to right: equal-area projections of the isolated overprint directions from both limestone and volcaniclastic rocks in geographic coordinates; ChRM directions of the limestones from all groups (Kioto Groups, Laptal Formation, and Dangar Formation) acquired by line fits in geographic coordinates; ChRM directions acquired by line fits in stratigraphic coordinates; ChRM directions of the limestones acquired by both line fits and great circle analysis. (e) Same equal-area projections of the isolated ChRM directions from Wölong Formation volcaniclastic rocks as in Figures 3a–3c. K and A_{95} are the concentration parameter and angular radius of 95% confidence of the mean observed Virtual Geomagnetic Pole, respectively.
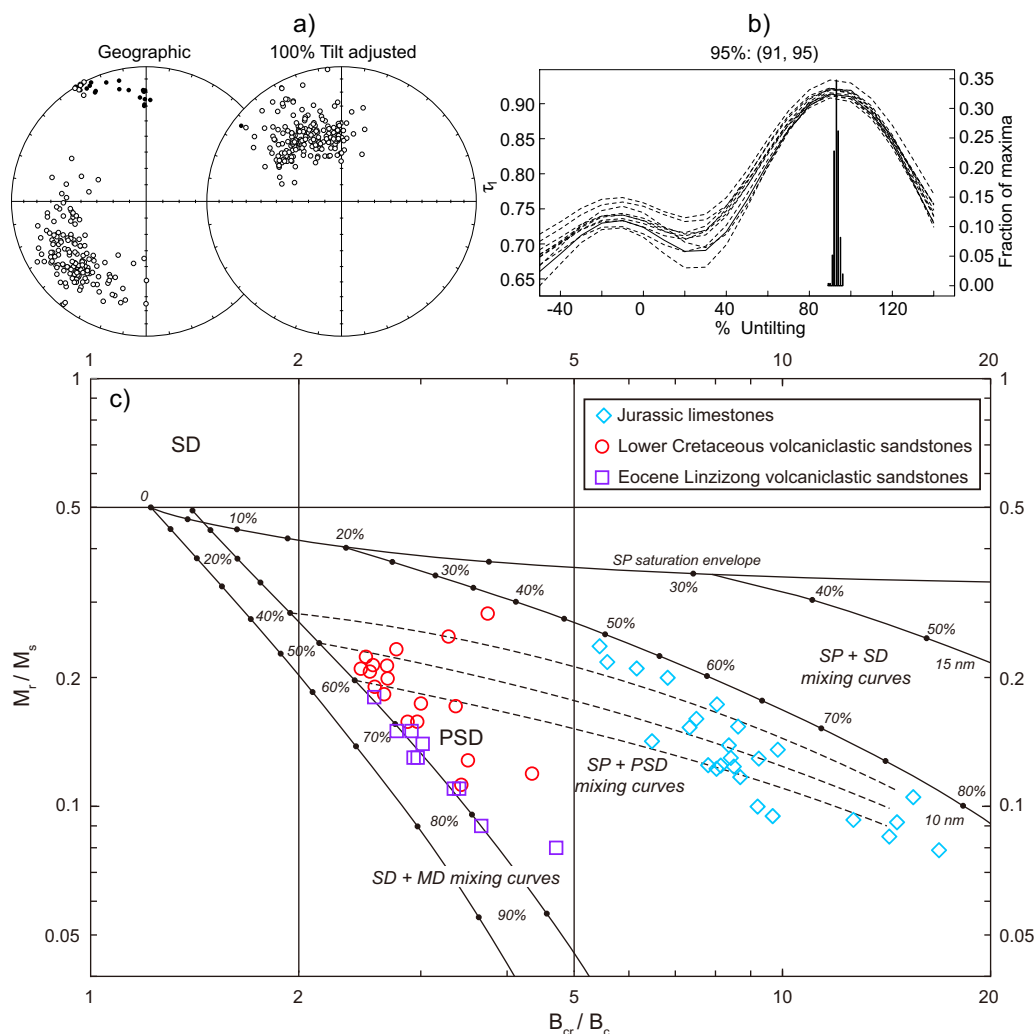
Figure 4. (a) Nonparametric fold tests [*Tauxe and Watson*, 1994] on the Jurassic limestones. Equal-area plots of the individual ChRM directions from each limestone specimen in (left) geographic and (right) stratigraphic coordinates. Before tilt correction, the ChRM directions of samples from the two limbs of the syncline are in two different groups. After tilt correction, the two groups cluster. (b) Results of the fold test with bootstrapped statistics on the first eigenvalues (τ_1) upon progressive untilting. The 95% bootstrap error interval is indicated. Best grouping is reached at 91–95% untilting. (c) Day plot [*Day et al.*, 1977; *Dunlop*, 2002b] of 43 limestone samples and 18 volcaniclastic specimens. Also plotted are 10 volcaniclastic specimens from the Eocene Linzizong Group in the Linzhou basin that retain a primary remanence [*Huang et al.*, 2013].

Thermomagnetic runs of specimens from the Jurassic limestones show very low initial magnetization intensities (5×10^{-3} to 1×10^{-2} Am^2/kg, Figures 5a–5e). Typical results for these specimens show an irreversible decrease in magnetization up to ∼580°C (Figures 5a–5c). These specimens are also characterized by a distinctly steeper decrease in magnetization slope of the thermomagnetic runs in the temperature range of ∼520–580°C, close to the Curie temperature of magnetite (∼580°C).

The initial magnetization intensity of the Lower Cretaceous volcaniclastic specimens is much higher (2×10^{-2} to 7×10^{-2} Am^2/kg) than that of the Jurassic limestones (Figures 5d and 5e). The hyperbolic shape of the thermomagnetic curves indicates a dominant paramagnetic component for nearly almost all of the specimens. All of the specimens show an irreversible decrease in magnetization with increasing temperature up to ∼580°C, which is typical for magnetite. Some specimens are also characterized by an increase in magnetization above ∼430°C, consistent with the oxidation of an iron sulfide. At this temperature, weakly magnetic or nonmagnetic iron sulfide often transforms into magnetite. It is likely that the aberrant NRM behavior observed during thermal demagnetization at >450°C is caused by this neoformed magnetic phase (Figure 5e).
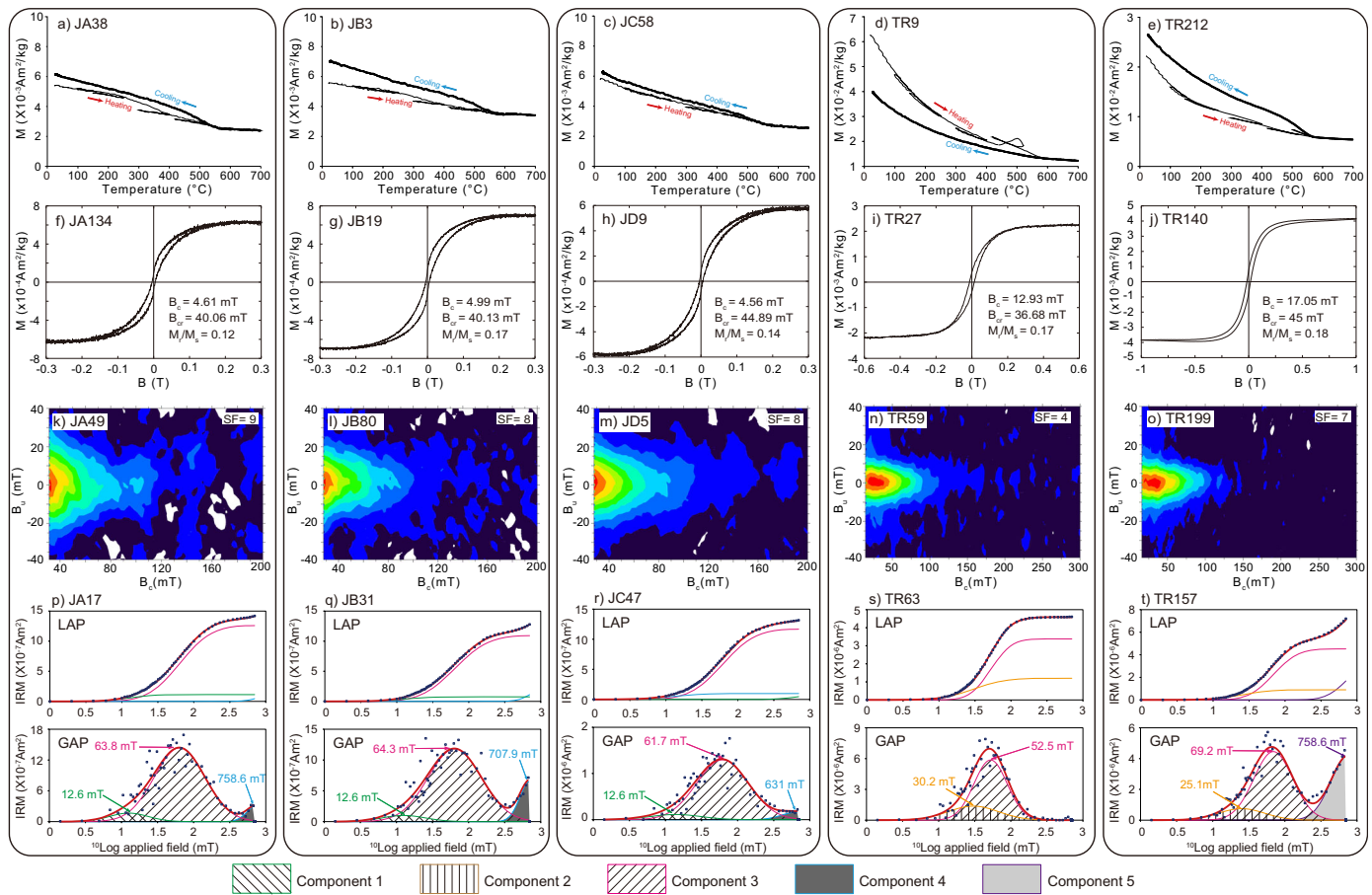
Figure 5. Rock magnetic results of the limestones and volcaniclastic sandstones. (a–e) High-field thermomagnetic runs on a modified horizontal translation Curie balance for typical samples from both Jurassic limestones (Figures 5a–5c) and Lower Cretaceous volcaniclastic rocks (Figures 5d and 5e). (f–o) Hysteresis loops and first-order reversal curve (FORC) diagrams for characteristic samples from both Jurassic limestones (loops: Figures 5f–5h; FORC: Figures 5k–5m) and Lower Cretaceous volcaniclastic sandstones (loops: Figures 5i and 5j; FORC: Figures 5n and 5o). Hysteresis loops are corrected for the paramagnetic contribution. FORC diagrams were produced using an in-house developed program (FORC_Analysis.exe, by Tom Mullender) at the "Fort Hoofddijk" Paleomagnetic Laboratory. For each sample, the optimal smoothing factor (SF) was calculated and applied based on adequate signal-to-noise ratios [*Roberts et al.*, 2000]. (p–t) IRM component analysis [*Kruiver et al.*, 2001] of representative limestone and volcaniclastic specimens. Squares are measured data points. The components are marked with different colored lines. Log_{10} ($B_{1/2}$) and DP are in log_{10} mT. LAP: linear acquisition plot and GAP: gradient acquisition plot.

5.2. Hysteresis Loops, IRM, and Back-Field and FORC Diagrams

Forty-three representative samples (11 from unit K_1, 7 from unit K_2, 2 from the Laptal Formation, 5 from the Dangar Formation, and 18 from the Wölong Formation) with masses ranging from 14 to 30 mg were mounted on a P1 phenolic probe and measured with MicroMag 2900 (supporting information Table S2). The procedure of the measurements and data processing are the same as that described in *Huang et al.* [2013]. Hysteresis parameters (M_s: saturation magnetization; M_r: saturation remanent magnetization; B_c: coercive force; and B_{cr}: remanent coercivity) were determined from the measurements.

Hysteresis loops for the samples from the Jurassic limestone specimens are wasp-waisted (Figures 5f–5h), which indicates the presence of two or more magnetic components with contrasting coercivities [*Jackson*, 1990; *Muttoni*, 1995; *Roberts et al.*, 1995] or different size fractions of a single mineral [*Tauxe et al.*, 1996]. B_c values of these specimens are very low, leading to high B_{cr}/B_c values (supporting information Table S2). The hysteresis data plot near the superparamagnetic (SP) + pseudosingle domain (PSD) mixing curves on a Day plot (Figure 4c) [*Day et al.*, 1977; *Dunlop*, 2002a, 2002b], suggesting that there are substantial amounts of SP-size particles in the specimens. The FORC diagrams for these specimens are characterized by contours that diverge away from the origin and spread along the B_u axis (Figures 5k–5m). This contour pattern is consistent with the behavior of typical interacting PSD magnetic particles [*Pike et al.*, 1999; *Roberts et al.*, 2000].

For most of the volcaniclastic specimens, the hysteresis loops are open and saturated by 300 mT (Figure 5i), indicating the dominance of a low-coercivity component. The hysteresis loops of a few specimens are

narrow and unsaturated at 1 T (Figure 5j), suggesting that some remanence is carried by a high-coercivity mineral, such as hematite or goethite. FORC diagrams for these specimens also have divergent and symmetrical contours with very low coercivities (Figures 6n and 6o), consistent with a population consisting predominantly of interacting PSD particles [*Pike et al.*, 1999; *Roberts et al.*, 2000]. This interpretation is consistent with magnetic grain sizes estimated with a Day plot (Figure 4c) [*Dunlop*, 2002a, 2002b].

5.3. IRM Component Analysis

We also semiquantitatively assessed the contributions of different magnetic minerals to the net magnetization with IRM component analysis. We follow the IRM-acquisition procedures described in *Huang et al.* [2013]. Nineteen representative specimens representing the entire section were analyzed using different components to fit the IRM-acquisition curves following the cumulative log-Gaussian approach [*Kruiver et al.*, 2001]. In general, all IRM-acquisition curves appear to be fit by five IRM components (increasing from magnetically soft to hard): component 1 with $B_{1/2}$ (the field at which half of saturation isothermal remanent magnetization (SIRM) is reached) of ∼13 mT and dispersion parameter (DP) of ∼0.30 (log units); a soft component 2 with $B_{1/2}$ ranging from 25 to 45 mT and DP varying from 0.25 to 0.45; a relatively hard component 3 with higher $B_{1/2}$ (50–70 mT) and notably variable DP (0.20–0.45); and much harder components 4 and 5 both with $B_{1/2} >400$ mT and variable DP (Figures 5p–5t and supporting information Table S3).

Components 1, 3, and 4 are used to fit the IRM-acquisition curves of the Jurassic limestones (Figures 5p–5r). Component 1 constitutes 4–10% of the SIRM. It is only required to fit the skewed-to-the-left distribution of component 3 and is interpreted to be thermally activated component 3 particles. Component 3 typically represents magnetite. It is the predominant magnetic carrier in the limestone specimens and contributes >60% to the SIRM. Component 4 is not close to saturation at the maximum applied field of 700 mT. It is normally interpreted to be hematite (or goethite). However, careful inspection of the limestones indicates that all of the specimens are dark blue, which is inconsistent with reddish hematite or yellowish goethite. We suggest that component 4 represents very fine-grained magnetite, close to the SP threshold size; clusters of magnetically interacting SP magnetite particles can remain unsaturated at 2 T, as described by *Dekkers and Pietersen* [1992]. This interpretation is in line with the above thermomagnetic and hysteresis analyses.

Components 2, 3, and 5 are required to fit the IRM curves of the specimens from the Lower Cretaceous volcaniclastic sandstones (Figures 5s and 5t). Component 2 with a lower $B_{1/2}$ than component 3 also represents magnetite, but of smaller grain size relative to component 3 magnetite. Component 5 (with a $B_{1/2}$ as high as component 4) is also not saturated by 700 mT. We interpret this component as hematite (or goethite), which is consistent with the yellowish color in outcrop and with the results from the hysteresis analyses described above.

In summary, these interpretations of the IRM component analysis are consistent with results from the other rock magnetic experiments. We conclude that the magnetization of specimens from the Jurassic limestones is carried by magnetite of variable grain size. The predominant magnetic carrier in specimens from the Lower Cretaceous volcaniclastic sandstones is magnetite, with hematite or goethite as a minor magnetic carrier.

6. End-Member Modeling of Magnetic Components

To illustrate the mechanism of remanence acquisition and to detect the potential remagnetization of the Jurassic to Lower Cretaceous Tethyan Himalaya sedimentary rocks from the studied section, we applied the end-member modeling method developed by *Gong et al.* [2009]. End-member modeling is based on the assumption that measured data are a linear mixture of a number of invariant constituent components, termed end-members. Several case studies demonstrate how powerful it can be for diagnosing remagnetization in both sedimentary and volcanic rocks [*Gong et al.*, 2009; *Van Hinsbergen et al.*, 2010; *Meijers et al.*, 2011; *Aben et al.*, 2014].

IRM-acquisition curves of 120 specimens from Jurassic limestones (48 from unit K_1, 24 from unit K_2, 25 from the Laptal Formation, and 23 from the Dangar Formation) and 104 samples from Lower Cretaceous volcaniclastic sandstones representing the entire section were measured. Procedures of the measurement and data analysis are described in *Aben et al.* [2014].

6.1. Jurassic Limestone Units

For Jurassic limestone specimens, the end-member curves become noisy with three or more end-members (Figures 6a and 6b), indicating that the data set is overinterpreted for those numbers of end-members.
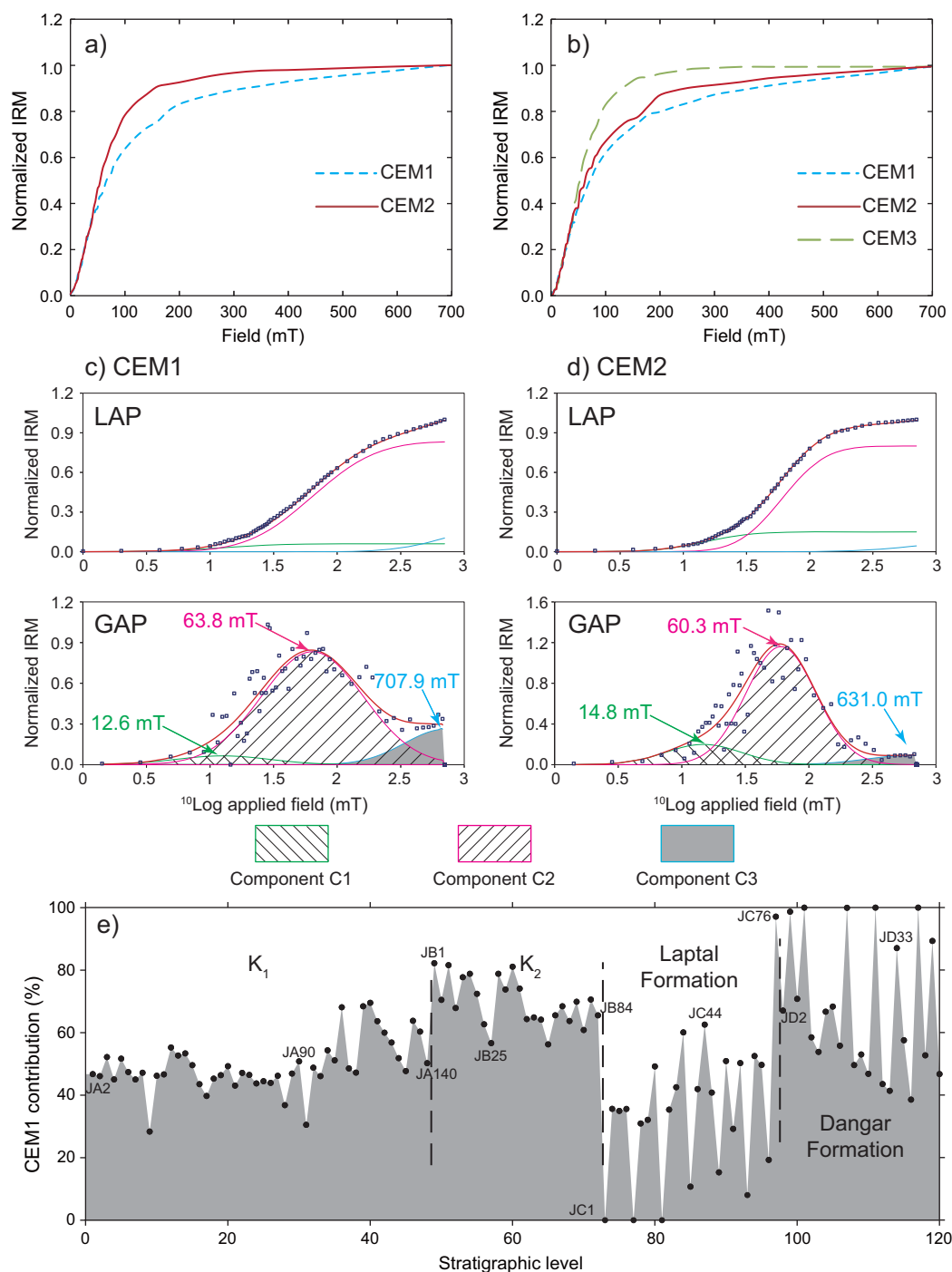
Figure 6. End-member modeling for the Jurassic limestones. (a and b) End-member modeling for the normalized IRM-acquisition curves with two (Figure 6a) and three (Figure 6b) end-members. (c and d) IRM component analysis [*Kruiver et al.*, 2001] of the end-members in our preferred two end-member model. (e) Plotting of the percentages of the CEM1 contribution to the SIRM for each specimen against stratigraphic level. The distance between the adjacent samples is arbitrarily set at 1; the sample codes progress up section in each sampled unit.

Comparison of the two end-member model with the three end-member model shows that the curves of end-member 1 (CEM1, C stands for "carbonate") in both models are identical, whereas the curve of end-member 2 (CEM2) in the two end-member model splits into CEM2 and CEM3 in the three end-member model (Figures 6a and 6b). This means that the three end-member model does not discriminate clearly more distinctive and geologically interpretable end-members than the two end-member model. We therefore prefer the two end-member model to interpret our data set from the Jurassic limestones.

We applied IRM component analysis to these two end-members (CEM1 and CEM2 in the two end-member model) [*Kruiver et al.*, 2001]. Three components (components C1, C2, and C3, increasing from soft to hard magnetically) are required to fit the normalized IRM-acquisition curves of the two end-members. Both CEM1 and CEM2 can be fit with these three components (Figures 6c and 6d). Component C1 is a very low-coercivity component (with $B_{1/2} \sim 13$ mT), which can be interpreted as thermally activated component C2 particles. Its contribution to the SIRM is minor ($\sim$5% for CEM1 and $\sim$15% for CEM2) (supporting information Table S3). Component C2 ($B_{1/2}$ of $\sim$60 mT) typically represents magnetite [*Day et al.*, 1977; *Lowrie*, 1990]. It is the dominant magnetic component for both CEM1 and CEM2 and contributes >75% to the SIRM (supporting information Table S3). Component C3 has a very high $B_{1/2}$ (>600 mT). Considering that the limestones are dark blue rather than reddish or yellowish, we interpret this component to represent clustered SP magnetite rather than hematite or goethite. Clustered SP magnetite of a few nanometers in size cannot be saturated even by 2 T [*Dekkers and Pietersen*, 1992; *Gong et al.*, 2009]. It contributes $\sim$20% to the SIRM for CEM1 and $\sim$8% to the SIRM for CEM2 (supporting information Table S3). These interpretations are similar to the IRM-acquisition curve-fitting results described in our rock magnetic studies above and are consistent with other rock magnetic analyses. This implies that the two end-members in our model are geologically interpretable.

Most specimens from the Jurassic limestone units are mixtures of CEM1 and CEM2 (Figure 6e). Contributions of CEM1 for specimens from each unit are distinct from other units. CEM1 contributes $\sim$50% and $\sim$70% to the SIRM for specimens from units K_1 and K_2, respectively. The contribution of CEM1 varies notably for specimens from the Laptal Formation and the Dangar Formation. There are also several specimens that plot on the baseline (specimens from the Laptal Formation) or the top-line (specimens from the Dangar Formation), indicating the sole contribution from CEM1 or CEM2 (Figure 6e), respectively.

6.2. Lower Cretaceous Volcaniclastic Sandstones

A two end-member model is also preferred for the interpretation of the data set for the Lower Cretaceous volcaniclastic rocks (Figures 7a and 7b). The normalized IRM-acquisition curves of the two end-members (VEM1 and VEM2, V stands for "volcaniclastics") can be fit with four components (components V1, V2, V3, and V4, increasing from soft to hard magnetically) (Figures 7c and 7d and supporting information Table S4). Components V1, V2, and V3 ($B_{1/2}$ of $\sim$25 mT, $\sim$50 mT, and $\sim$70 mT, respectively) typically represent magnetite with different grain sizes [*Day et al.*, 1977; *Lowrie*, 1990]. Component V1 has low contribution to the SIRM in both VEM1 and VEM2, whereas components V2 and V3 are the main magnetic component for VEM1 and VEM2, respectively. Component V4 (with very high $B_{1/2}$ of $\sim$800 mT) is interpreted to be hematite or goethite, as inferred by the yellowish color of some specimens; it contributes $\sim$25% to the SIRM for VEM1.

The contribution of VEM1 varies notably for the volcaniclastic specimens (Figure 7e). For the lower part (stratigraphic level: TR1-TR119), VEM1 has a lower average contribution (9%; Figure 7e). Up section, the contribution of VEM1 increases up to 100% (TR157) in the middle interval (stratigraphic level: TR122-TR163), and then it decreases sharply but is still as high as 45% on average in the upper interval (stratigraphic level: TR165–TR266; Figure 7e). Considering that the contribution of hematite (or goethite) to the SIRM of VEM1 is $\sim$25%, the high percentages of VEM1 for the middle and upper parts of the sampled volcaniclastic rocks indicate that hematite (or goethite), often produced by late-stage weathering in outcrop, is widespread in the rocks as magnetic carrier. This may explain the erratic demagnetization behavior of some specimens from the middle and especially the upper parts of the volcaniclastic unit.

7. SEM Observation and EDS Analysis

We analyzed thin sections of both Jurassic limestones and Lower Cretaceous volcaniclastic sandstones with the SEM to identify textural relationships and diagenetic conditions of magnetic minerals. EDS analysis was applied to obtain compositional information. Ten representative limestone specimens (JA15, JA29, JA49, JB49, JB80, JC9, JC58, JC77, JD7, and JD40) and seven volcaniclastic sandstone specimens (TR27, TR63, TR121, TR199, TR212, TR252, and TR261) were investigated on a Hitachi S3400 SEM, operated at 20 keV and 40–60 nA at the Electron Microscope Unit at the University of Hong Kong (China).

Two different morphologies of magnetic minerals are generally present in the Jurassic limestone samples (Figures 8a–8l). We interpret both phases to be magnetite based on the EDS analysis (supporting
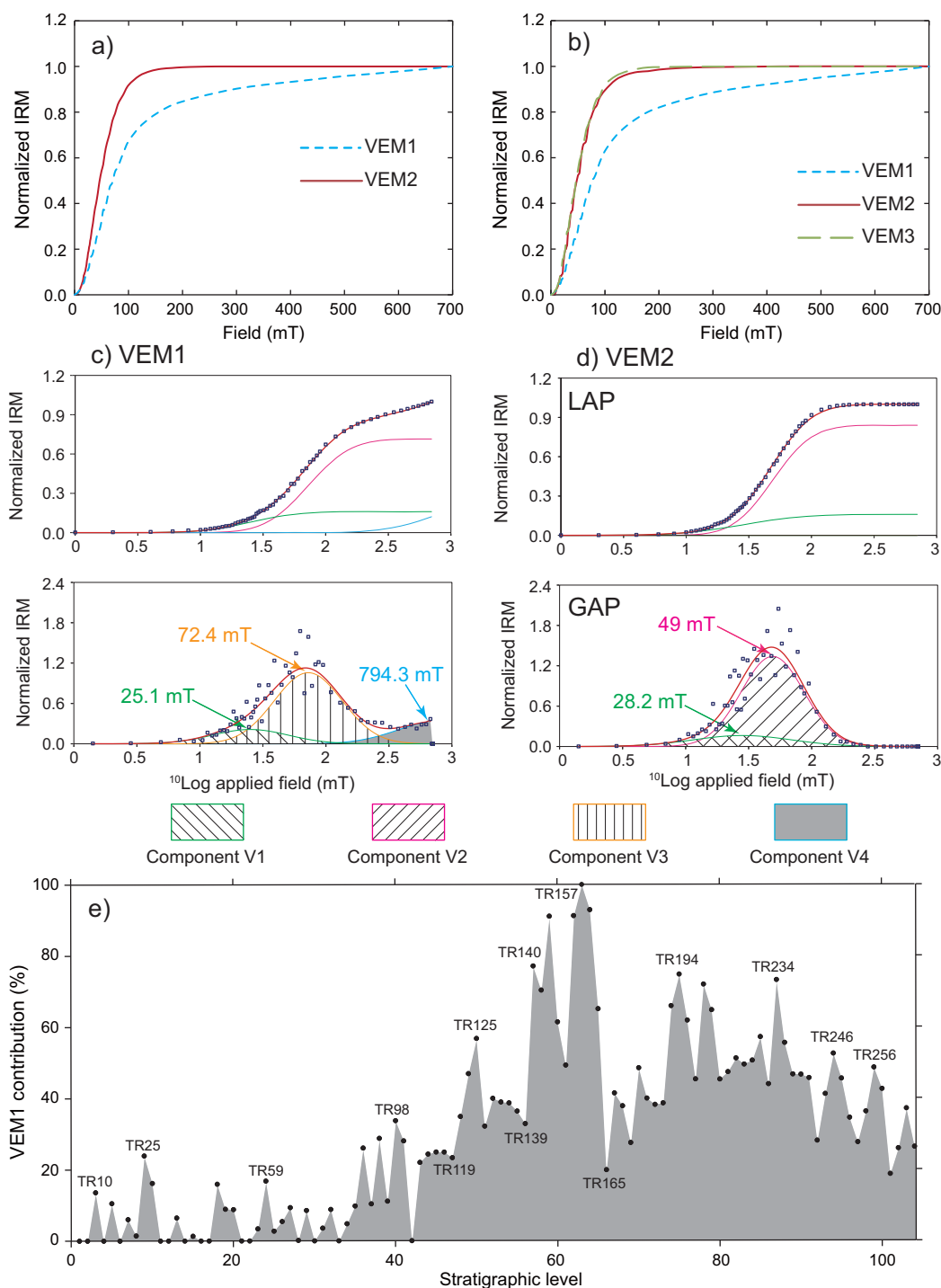
Figure 7. End-member modeling for the Lower Cretaceous volcaniclastic sandstones. (a and b) End-member modeling for the normalized IRM-acquisition curves with two (Figure 7a) and three (Figure 7b) end-members. (c and d) IRM component analysis [*Kruiver et al.*, 2001] of the end-members in our preferred two end-member model. (e) Plotting of the percentages of the VEM1 contribution to the SIRM for each specimen against stratigraphic level. The distance between the adjacent samples was arbitrarily assumed to be "1"; the sample codes increase up section in each sampled unit. Hematite (or goethite) contributes ~25% to the SIRM of VEM1, more contribution of VEM1 in the specimen indicates more hematite (or goethite) formed by stronger alteration and weathering; see details in the text.

information Figures S1a–S1m) and the rock magnetic results described in the previous sections. One phase is characterized by small (<10 μm) crystals (Figures 8a–8c, 8e, 8g, and 8i). This population is widespread and is usually distributed in the calcite matrix (Figures 8a, 8e, 8g, and 8i), with a secondary Ti-O matrix
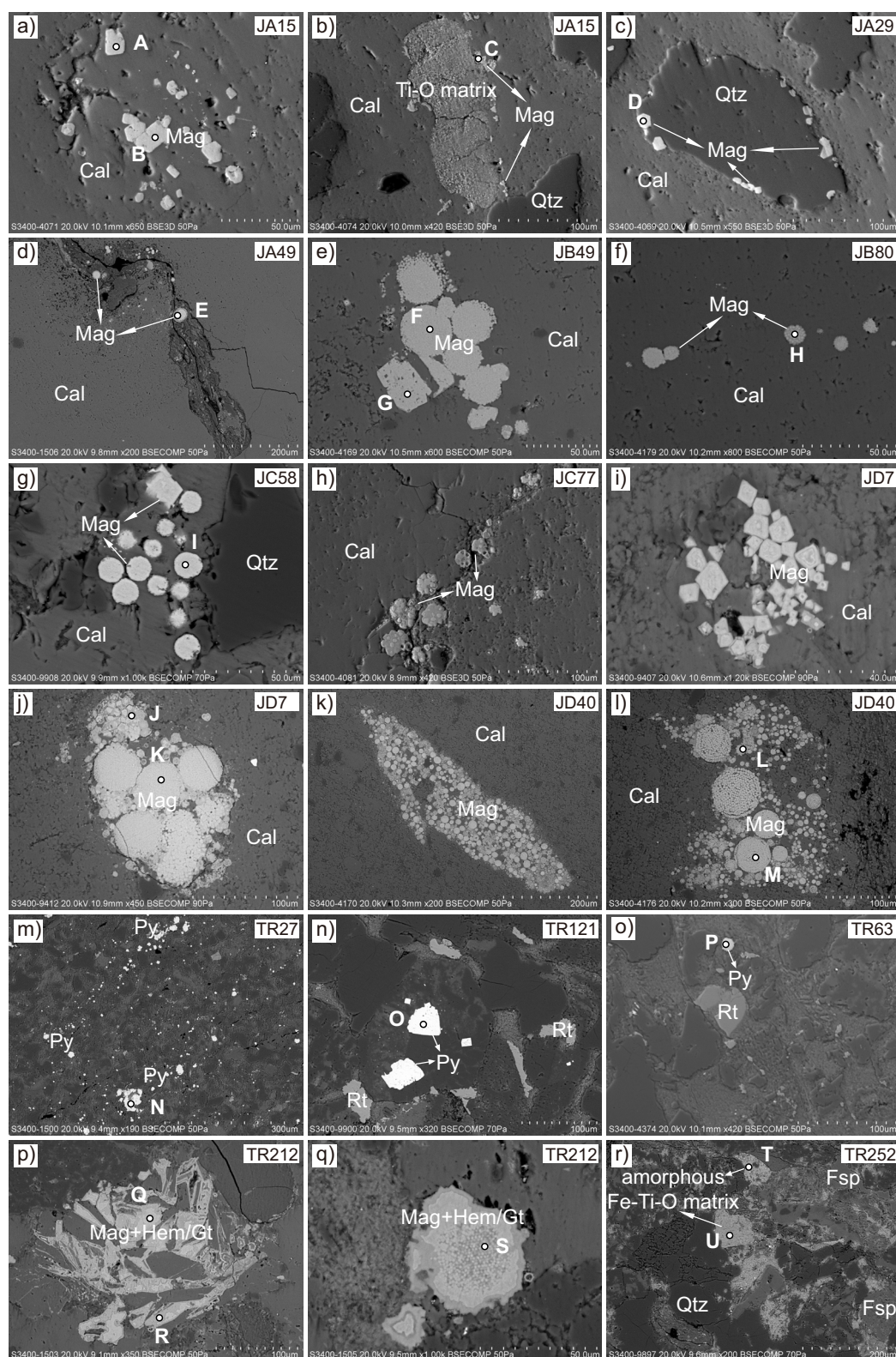
Figure 8. SEM back-scattered electron images for selected samples of (a–l) Jurassic limestone and (m–r) Lower Cretaceous volcaniclastic sandstones. Mag: magnetite, Cal: calcite, Qtz: quartz, Py: pyrite, Rt: rutile; Hem: hematite; Gt: goethite; and Fsp: feldspar. White dots indicate EDS analysis spots; analyses provided in supporting information Figure S1.

(Figure 8b), or around quartz grains (Figure 8c). Authigenic growth-zoning and rims are observed in some grains (Figure 8i). Some grains are pseudomorphs after euhedral pyrite and are most likely an oxidation product of pyrite (Figures 8e and 8g) [*Suk et al.*, 1990a]. These euhedral magnetite grains probably grew during later diagenetic processes [*Suk et al.*, 1990b; *Weil and Van der Voo*, 2002]. A second phase is framboidal with individual framboid sizes ranging from only a few μm to >50 μm (Figures 8d–8h and 8j–8l). The framboids occur in the calcite matrix (Figures 8e–8g and 8j–8l) or along cracks (Figures 8d and 8h). They are the dominant form of magnetite in most limestone specimens. Although framboids are the common textural form of pyrite and greigite in sedimentary rocks [*Wilkin et al.*, 1996; *Rowan and Roberts*, 2005, 2006], we did not detect iron sulfides in our limestone specimens (supporting information Figures S1a–S1m). This indicates that the framboidal magnetite in the Jurassic limestones was formed by replacement of early diagenetic pyrite or greigite [*Suk et al.*, 1990a; *Roberts et al.*, 2011]. These framboids are comprised of large numbers of small (<1 μm) magnetite crystallites and can therefore be a stable remanence carrier.

For the Lower Cretaceous volcaniclastic sandstones, most specimens do contain iron sulfides, which is consistent with what we determined from the thermomagnetic experiments (Figures 8m–8o and supporting information Figures S1n–S1p). The EDS analysis indicates an Fe:S ratio of ∼1:2, which suggests that the iron sulfide is pyrite (supporting information Figures S1n–S1p). These pyrite grains are usually subhedral to euhedral with grain sizes of a few μm to 50 μm (Figures 8m and 8n). Framboidal pyrite is also observed (Figure 8o). In some specimens, however, the observe iron oxide grains are pseudomorphic after subhedral-euhedral or framboidal pyrite with a reaction rim (Figures 8p and 8q), which suggests that they formed as a consequence of oxidation of preexisting pyrite as in the Jurassic limestones [*Suk et al.*, 1990a; *Roberts et al.*, 2011]. An amorphous Ti-O matrix is abundant in these samples (Figure 8r).

8. Discussion

8.1. Remagnetization of the Jurassic Limestones

The lower limestone interval of the studied section was biostratigraphically dated to the Pliensbachian through Oxfordian (190–160 Ma) [*Jadoul et al.*, 1998]. This time interval is characterized by many geomagnetic reversals [*Gradstein et al.*, 2012]. The ChRM directions from the Jurassic limestones, however, are exclusively of normal magnetic polarity (Figures 2 and 3), which is a strong indication that the rocks may be remagnetized.

Rock magnetic tests described above show that the predominant ferromagnetic mineral in the Jurassic limestones is magnetite in the SP to PSD size range. Although the SP population of magnetite cannot be the carrier of NRM, it has long been associated with remagnetization in limestones [e.g., *Jackson*, 1990; *McCabe and Channell*, 1994; *Suk and Halgedahl*, 1996; *Dunlop*, 2002b; *Jackson and Swanson-Hysell*, 2012]. Dispersed SP magnetite particles can be saturated in fairly low fields, leading to wasp-waisted hysteresis loops [*Tauxe et al.*, 1996; *Fabian*, 2003], which are similar to the loops observed in the Jurassic limestones described here (Figures 5f–5h). On a Day plot, all of the limestone specimens plot in the same SP + SD (single domain) or SP + PSD region (Figure 4c) that is characteristic for remagnetized limestones [*Jackson*, 1990; *McCabe and Channell*, 1994; *Xu et al.*, 1998; *Dunlop*, 2002b; *Elmore et al.*, 2006; *Jackson and Swanson-Hysell*, 2012]. In contrast, limestones with demonstrably primary magnetization usually plot in the SD + MD region and do not have a significant SP contribution [*Channell and McCabe*, 1994; *Tarduno and Myers*, 1994; *Belkaaloul and Aïssaoui*, 1997; *Abrajevitch and Kodama*, 2009; *Ménabréaz et al.*, 2010; *Jackson and Swanson-Hysell*, 2012; *Roberts et al.*, 2013]. Limestones with a substantial SP contribution (and thus with hysteresis characteristics indicating complete remagnetization) could possibly carry a primary NRM when the magnetic particles are extraterrestrial in origin or formed by magnetotactic bacteria during or immediately following deposition [e.g., *Freeman*, 1986; *Lanci and Kent*, 2006; *Lanci et al.*, 2007; *Kopp and Kirschvink*, 2008; *Lanci et al.*, 2008; *Moskowitz et al.*, 2008]. The magnetite in our limestones does not exhibit characteristics of either of these origins, but are instead formed as pseudomorphs after pyrite (Figure 8).

Our end-member modeling helps identify potential mechanisms for the remanence acquisition (Figure 6) and helps evaluate and compare the rock magnetic properties of a large number of specimens from the whole section. Guided by the rock magnetic analyses, both of the two end-members in our preferred two end-member models are interpreted to be a combination of PSD and clustered SP magnetite. The two end-members (CEM1 and CEM2) for the Jurassic limestones are similar to the two end-members (end-member 2

and end-member 1, respectively) in the remagnetized limestones in the Organyà basin (Spain) presented by *Gong et al*. [2009].

Our interpretation of the end-members is bolstered by the SEM observations and EDS analyses. IRM component analysis of the end-members showed that PSD magnetite has a dominant contribution of ∼75% to SIRM in both CEM1 and CEM2. Given that SP magnetite cannot carry the NRM, PSD magnetite (inferred from the Day plot and observed with the SEM) should be the unique carrier of the NRM in the Jurassic limestones. The euhedral or framboidal shape of the PSD magnetite, however, indicates that the observed magnetite grains are authigenic and therefore clearly secondary (Figure 8). Although we cannot assess the contribution of the observed secondary magnetite to the NRM, the SEM evidence indicates that secondary magnetite is abundant and we therefore interpret it as the principal magnetic carrier. We note that primary detrital magnetic particles in limestones are usually low, and it often dissolved by reductive dissolution prior to lithification [*Karlin and Levi*, 1983; *Freeman*, 1986; *Tarduno*, 1995; *Smirnov and Tarduno*, 2001].

In summary, ChRM direction analyses, rock magnetic tests, end-member modeling, and SEM and EDS studies lead us to conclude that the Jurassic limestones are remagnetized. The positive fold test indicates that the ChRMs from the Jurassic limestones of the section have a prefolding origin. The mean direction indicates that remagnetization occurred at 23.8°S [21.8°S, 26.1°S] (95% confidence) latitude.

8.2. Primary NRM in the Lower Cretaceous Volcaniclastic Rocks

Detailed rock magnetic analyses indicate that PSD magnetite is the dominant magnetic carrier of the volcaniclastic rocks, whereas hematite or goethite (or both) produced during late-stage weathering in outcrop has a minor contribution to the NRM. The hysteresis loops of the volcaniclastic rocks are generally open rather than wasp-waisted (as is common for remagnetized limestones [*Jackson and Swanson-Hysell*, 2012]) (Figure 5i). Most of the volcaniclastic sandstones plot along the single domain (SD) + multidomain (MD) mixing line in the PSD region and not along an SP mixing curve (Figure 4c). This trend is similar to specimens from the Linzizong volcaniclastic sandstones in the Linzhou basin that carry a demonstrably primary magnetization [*Huang et al*., 2013], as well as to nonremagnetized limestones [*Jackson and Swanson-Hysell*, 2012; *Roberts et al*., 2013]. Moreover, the magnetic properties of the Lower Cretaceous volcaniclastic sandstones are very different from the underlying Jurassic limestones, as well as demonstrably remagnetized limestones elsewhere (Figure 4c) [*Jackson*, 1990; *McCabe and Channell*, 1994; *Xu et al*., 1998; *Weil and Van der Voo*, 2002; *Elmore et al*., 2006; *Gong et al*., 2008].

Although VEM1 in our preferred two end-member model of the volcaniclastic samples has a similar IRM-acquisition curve to CEM1 of the Jurassic limestone samples, its magnetic significance is quite different (Figure 7). Moreover, the contribution of VEM1 to the SIRM of the volcaniclastic samples is generally lower than that of CEM1 to the SIRM of the limestone samples (Figure 6e). We also note that VEM2 in the volcaniclastic specimens is remarkably different from CEM2 of the limestone: VEM2 is completely saturated below 200 mT, whereas CEM2 saturates above 400 mT (Figures 6a and 7a). The two end-members (VEM1 and VEM2) from the Lower Cretaceous volcaniclastic sandstones are comparable to the two end-members (end-member 3 and end-member 2, respectively) in the nonremagnetized limestones and blue clay in the Bey Dağları region of Turkey [*Van Hinsbergen et al*., 2010].

Our end-member modeling also provides a stratigraphic view of the generalized rock magnetic characteristics of the entire sampled volcaniclastic section (Figure 7e). It confirms that magnetite is the dominant magnetic carrier, as also indicated from other rock magnetic tests, and it also gives a semiquantitative estimation of the hematite/goethite contribution, which can be used to evaluate of degree of alteration/weathering in the volcaniclastic specimens. High magnetic contributions from hematite or goethite may explain why a stable ChRM is only rarely be isolated from some specimens in the middle and upper parts of the volcaniclastic section. This alteration and weathering, however, are distinct from the remagnetization displayed by the Jurassic limestones; it did not occur across the entire volcaniclastic section, and we infer that alteration occurred only after the rocks were at the surface. In contrast, the remagnetization of the Jurassic limestones is pervasive and took place much earlier and before tectonic deformation.

The results of the rock magnetic tests and of the end-member modeling are further confirmed by SEM observation and EDS analysis. The detected iron sulfide in the thermomagnetic experiment of most samples is clearly pyrite (Figures 8m–8o and supporting information Figures S1n–S1p). This paramagnetic mineral

plays no role in the remanence acquisition, but it can easily transform to magnetite, hematite, or goethite, which do carry remanence [*Cairanne et al.*, 2004]. Unlike the remagnetized Jurassic limestones, which contain no iron sulfides, pyrite is widespread in most volcaniclastic samples. We argue that the dominant magnetic carrier in the volcaniclastic sandstones is detrital magnetite. Its grain size was probably reduced by reductive dissolution during early diagenesis and it is therefore below the resolution of SEM. In other volcaniclastic specimens, however, iron sulfide was not detected in either rock magnetic studies or EDS analysis. Careful inspection indicates that preexisting iron sulfides in those samples have been oxidized to iron oxides (Figures 8p, 8q and supporting information Figures S1q–S1s). End-member modeling also indicates that magnetite is the main remanence carrier, but hematite, goethite or both also contribute to the SIRM in these specimens. The erratic demagnetization trajectories of these specimens may thus be caused by the transformation of pyrite to secondary magnetite and hematite or goethite during later weathering. These newly formed magnetic minerals would contaminate the magnetic signal of the primary detrital magnetite.

Although no paleomagnetic field test can be completed in the given Wölong Formation, we applied detailed rock magnetic analyses, end-member modeling, SEM, and EDS investigations to constrain the mechanism of the remanence acquisition of the volcaniclastic sandstones. Our data consistently indicate that the Lower Cretaceous volcaniclastic sandstones carry largely a primary remanent magnetization, with some alteration and weathering in the upper part of the sampled volcaniclastic section. In the inferred depositional age span, the inclination of the mean ChRM directions of the volcaniclastic sandstones fits well with the global apparent polar wander path (GAPWaP) of India, and after the earliest Cretaceous, India has never been at latitudes as low as indicated by the Wölong volcaniclastic rocks [*Torsvik et al.*, 2012].

8.3. Timing of the Remagnetization and Tectonic Consequences

In an attempt to constrain the timing of the remagnetization of the Jurassic limestones, we plot the mean ChRM direction obtained from the Jurassic limestones on the declination and inclination plots of the GAPWaP curve of India at the coordinate of the studied section (Figure 9 and supporting information Table S4) [*Torsvik et al.*, 2012]. We can estimate the timing of remagnetization in two ways.

First, we can assume that the studied section has not been rotated relative to India. The limestones record a declination of $334.2 \pm 2.4°$, which corresponds to the predicted declination of India for an age range of 103–84 Ma (Figure 9). In this correlation, the observed inclination ($-41.5 \pm 2.9°$) is shallower than predicted by GAPWaP in Indian coordinates. That is, if we fix declination to the GAPWaP, then the observed inclination suggests that the Tibetan Himalaya were located 1280 ± 260 km north of their present relative position to India.

Alternatively, we can assume that the Tibetan Himalaya was rigidly attached to India. The inclination recorded in the limestones ($-41.5 \pm 2.9°$) corresponds to the predicted inclination of India for an age range of 77–67 Ma (Figure 9). In this scenario, the observed declination suggests that the studied section has been rotated $19.4 \pm 3.0°$ counterclockwise since remagnetization.

The normal polarity observed in the Jurassic limestones is consistent with remagnetization from 103 to 84 Ma (during the Cretaceous Normal Superchron) (Figure 9). For the 77–67 Ma interval required by Scenario 2, only intervals of 77–74.3, 73.7–72, and 69–67 Ma correspond to periods of normal polarity on the GPTS [*Gradstein et al.*, 2012].

Scenario 1 assumes no rotation, whereas Scenario 2 requires $19.4 \pm 3.0°$ of counterclockwise rotation of the section relative to India. It is difficult to independently test the rotation of the Tibetan Himalaya relative to India during India-Asia collision, but some data have been published. *Patzelt et al.* [1996] and *Yi et al.* [2011] studied uppermost Cretaceous and Paleogene marine carbonates from the Tibetan Himalaya to the north and east of our study area and found only minor amounts (5–15°) of clockwise rotation (Figure 9), whereas secondary magnetization acquired during collision show no systematic rotations, or only minor clockwise rotation [*Appel et al.*, 2012; *Crouzet et al.*, 2012; *Liebke et al.*, 2013].

Scenario 2 assumes no paleolatitudinal motion of the Tibetan Himalaya relative to India, whereas Scenario 1 requires $11.5 \pm 2.4°$ of paleolatitudinal separation between the studied section and India. Because the paleolatitude of the volcaniclastic sandstones is similar to the position predicted from the Indian GAPWaP, Scenario 1 predicts that the Tibetan Himalaya moved 1280 ± 260 km north relative to the Indian craton between the deposition of the sandstone and the remagnetization of the limestone. Other paleomagnetic
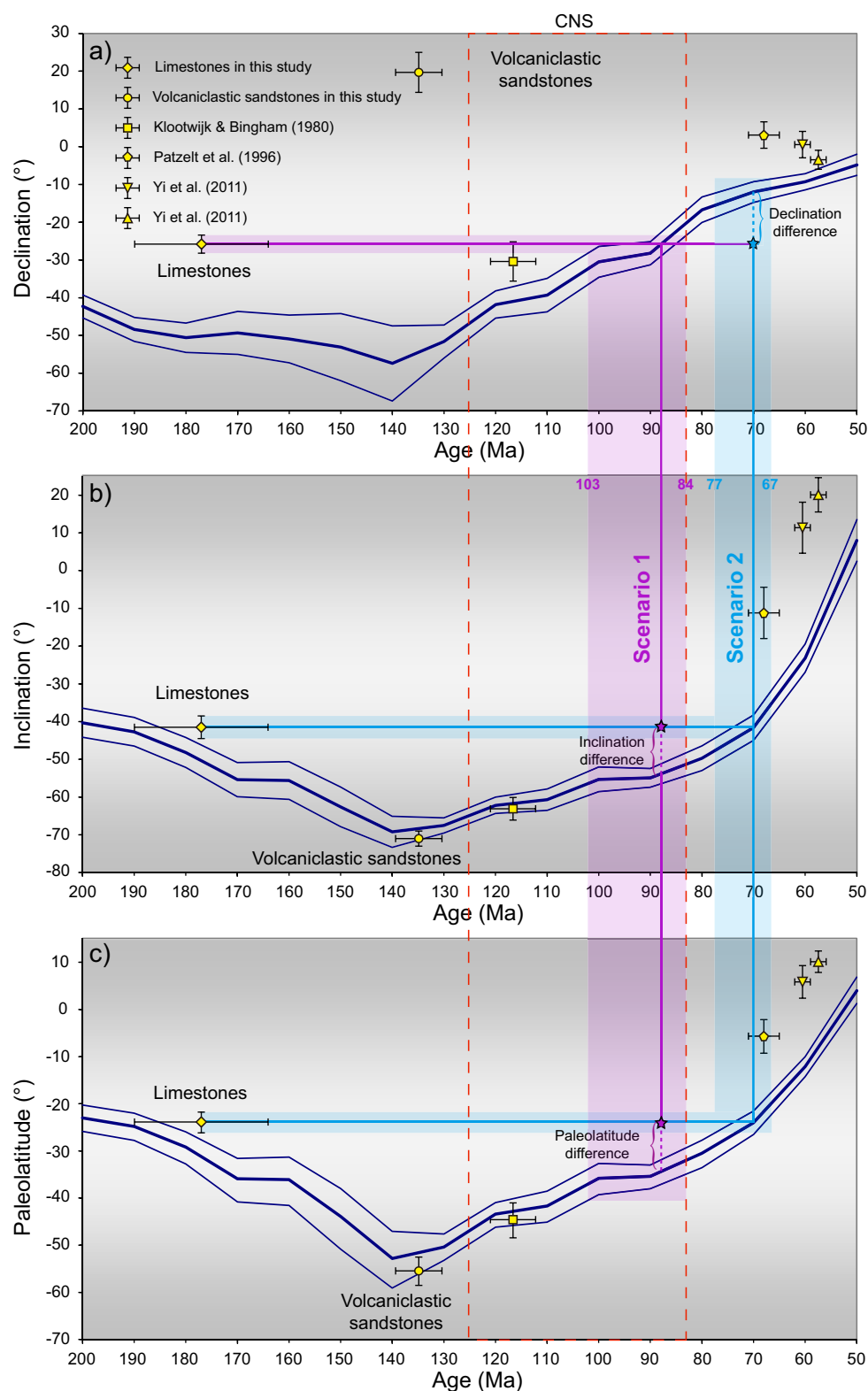
Figure 9. (a and b) Plots of the mean ChRM directions (declination and inclination, respectively) and (c) corresponding paleolatitudes determined from Jurassic limestones and Lower Cretaceous volcaniclastic sandstones on the GAPWaP curve of India [*Torsvik et al.*, 2012]. Two scenarios for the remagnetization are suggested by fixing either declination (Scenario 1, purple lines) or inclination (Scenario 2, blue lines) of the limestones to the GAPWaP of India (see discussion in the main text). The purple and blue bands represent the error bars. Red dashed box indicates the time interval of the Cretaceous Normal Superchron (CNS) [*Gradstein et al.*, 2012]. Previous Cretaceous paleomagnetic results from the Tibetan Himalaya [*Klootwijk and Bingham*, 1980; *Patzelt et al.*, 1996; *Yi et al.*, 2011] recalculated by *van Hinsbergen et al.* [2012] are also plotted.

studies from the Tibetan Himalaya have shown uppermost Cretaceous (Zongshan Formation: 71–65 Ma) and Paleogene (Zongpu Formation: 62–56 Ma) marine sedimentary rocks were deposited at ~20° of latitude farther north than predicted by the GAPWaP in Indian coordinates [*Patzelt et al.*, 1996; *Dupont-Nivet et al.*, 2010b; *Yi et al.*, 2011; *van Hinsbergen et al.*, 2012]. Thus, if the limestones were remagnetized as in Scenario 1, then approximately one half of the paleolatitudinal separation observed in the Paleogene rocks developed before 103–84 Ma. If instead the limestones were remagnetized as in Scenario 2, then those ~20° of latitudinal separation accumulated entirely between 77 Ma (maximum remagnetization time in Scenario 2) and 65 Ma (minimum deposition time of Zongshan Formation). This latter would require an extremely high rifting rate of ≥20 cm/yr (Figure 9 and supporting information Table S4).

The volcaniclastic sandstones were deposited at ~134 Ma, and, as described above, do not show evidence for remagnetization. Therefore, the clockwise rotation of ~77.1 ± 5.7° indicated by our paleomagnetic analysis of the volcaniclastic sandstones, must have accumulated after the Early Cretaceous deposition of the volcaniclastics, but before the Late Cretaceous remagnetization of the Jurassic limestones. This rotation is most easily attributed to the Early Cretaceous extension within the Tibetan Himalaya, evident from the stratigraphic and volcanic geochemical record [e.g., *Gaetani and Garzanti*, 1991; *Hu et al.*, 2010; *Garzanti and Hu*, 2014]. This rifting may also be responsible for the latitudinal separation required in Scenario 1 described above.

We emphasize that the timing of the remagnetization cannot be directly measured with information presented here, and that our correlations are based on several assumptions that are difficult to test independently. We are confident, however, that the Lower Cretaceous volcaniclastic sandstones are not remagnetized and that the inclinations preserved in these sediments indicate no significant paleolatitudinal separation between the Tibetan Himalaya and India at the start of the Early Cretaceous. Our results support the conclusions of *Klootwijk and Bingham* [1980], who studied similar but slightly younger volcaniclastic rocks a few hundred kilometers to the west.

8.4. Mechanisms for the Remagnetization of the Jurassic Limestones

Remagnetization can be caused by a variety of processes. For example, although thermoviscous resetting [*Kent*, 1985; *Harlan et al.*, 1996] is rather common, it is an unlikely mechanism for the remagnetization of the present Jurassic limestones (so as to the Lower Cretaceous volcaniclastic sandstones). No magmatic bodies are found near the section and the sedimentary rocks of the section underwent very low grade metamorphism with maximum postdepositional temperatures probably <200°C [*Garzanti et al.*, 1994; *Jadoul et al.*, 1998]. We also note that if metamorphism were responsible for the remagnetization, then it would be associated with the Northern Hemisphere India-Asia collision, but the remagnetization directions are demonstrably prefolding and indicating a Southern Hemisphere location. Our rock magnetic and petrographic analyses indicate that the Jurassic limestones were chemically remagnetized: the dominant magnetic carrier in the limestones is authigenic magnetite, which carries a chemical remanent magnetization (CRM).

Authigenic magnetite is common in remagnetized carbonates [e.g., *McCabe et al.*, 1983; *Suk et al.*, 1990a, 1990b, 1993; *Suk and Halgedahl*, 1996; *Weil and Van der Voo*, 2002]. It can form as an oxidation product of pyrite or other iron sulfides under the influence of externally derived fluid [e.g., *McCabe et al.*, 1989; *Suk et al.*, 1990a, 1991; *Fruit et al.*, 1995; *Elmore et al.*, 2001; *Zegers et al.*, 2003; *Rowan and Roberts*, 2006]. It can also grow in a closed sediment system such as during clay diagenesis (particularly the conversion of smectite to illite) or during organic maturation and pressure solution [e.g., *Jackson et al.*, 1988; *Katz et al.*, 2000; *Woods et al.*, 2002; *Zegers et al.*, 2003; *Blumstein et al.*, 2004; *Oliva-Urcia et al.*, 2008; *Tohver et al.*, 2008]. We observe large amounts of authigenic magnetite with pyrite pseudomorphs (part of the euhedral magnetite and all of the framboidal magnetite) in the Jurassic limestones (Figure 8). Therefore, we conclude that oxidation of iron sulfides to magnetite was the principal mechanism of remagnetization in the Jurassic limestones. This process was probably associated with fluid flow [*Elmore et al.*, 2012; *Jackson and Swanson-Hysell*, 2012], a conclusion supported by the observed distribution of some magnetite along cracks (Figures 8d and 8h). Some of the observed euhedral magnetite may have crystallized directly from the fluids (Figures 8a and 8c). Fluid-flow-driven oxidation and direct crystallization of magnetite from the fluid can also explain the formation of SP magnetite. Although SP magnetite can be created by iron-reducing bacteria [*Lovley et al.*, 1987] or during the reductive dissolution of primary detrital magnetite of PSD and MD size ranges [*Karlin and Levi*, 1983; *Tarduno*, 1995; *Smirnov and Tarduno*, 2001], it may also form during the oxidation of preexisting nanoparticles of iron sulfides.

The depositional environment of the Jurassic limestones and the redox conditions during deposition probably facilitated the remagnetization. *Jackson and Swanson-Hysell* [2012] found that samples that plot along the SD-MD mixing line largely come from pelagic limestones, in which detrital or bacterial magnetite can carry a primary remanence. The Jurassic limestones studied here, however, were largely deposited on a tropical continental shelf [*Jadoul et al.*, 1998] where the contribution of detrital magnetite was low because of low clastic influx and high carbonate saturation. Moreover, oceanic anoxic events occurred during the deposition of the carbonate successions (especially in unit K_2 of the Kioto Group [*Jadoul et al.*, 1998]), and we expect the precipitation of iron sulfides and ubiquitous reductive dissolution of any primary detrital or biogenic magnetite during these events. Bottom water redox conditions also changed repeatedly throughout the Cretaceous, as documented by black shales associated with Oceanic Anoxic Events (OAEs) [*Schlanger and Jenkyns*, 1976; *Jenkyns*, 1980; *Leckie et al.*, 2002; *Turgeon and Creaser*, 2008] and Cretaceous oceanic red beds (CORBs) [*Hu et al.*, 2005; *Wang et al.*, 2005; *Neuhuber et al.*, 2007; *Hu et al.*, 2009]. We suggest that during the deposition of CORBs, oxygen-rich seawater could have migrated along structural and stratigraphic surfaces (e.g., unconformities, synsedimentary faults, and fractures) or interconnected porosity. Percolation of the oxygenated bottom waters into the sediments could promote the transformation of early diagenetic pyrite to magnetite and induce the remagnetization of the Jurassic limestones. The thick black shale intervals frequently intercalated within the Lower Cretaceous volcaniclastic sandstones may have prevented the oxidizing fluids from circulating through the entire section, thereby insulating the more porous volcaniclastic sandstones from oxidation and remagnetization.

9. Conclusions

The Tibetan Himalaya section studied here, consisting of Jurassic limestones and Lower Cretaceous volcaniclastic sandstones, was deposited on the northern passive margin of the Indian subcontinent. In this paper, we applied paleomagnetic methods to this section to constrain the kinematic evolution of "Greater India" before the India-Asia collision. Our comprehensive paleomagnetic and rock magnetic analyses and microscopic investigations lead us to conclude that:

1. The Jurassic limestones yield a mean ChRM direction of $D_s \pm \Delta D_s = 334.2 \pm 2.4°$, $I_s \pm \Delta I_s = -41.5 \pm 2.9°$ ($n = 239$, $K = 18.5$, $A_{95} = 2.2°$), corresponding to a paleolatitude of 23.8°S [21.8°S, 26.1°S].

2. The ChRM of the Jurassic limestones has a prefolding/precollision, Southern Hemisphere origin.

3. The Lower Cretaceous volcaniclastic sandstones have a mean ChRM direction of $D_s \pm \Delta D_s = 19.7 \pm 5.3°$, $I_s \pm \Delta I_s = -71 \pm 2°$ ($n = 201$, $K = 11.9$, $A_{95} = 3°$), corresponding to a paleolatitude of 55.5°S [52.5°S, 58.6°S].

4. The magnetic carrier in the Jurassic limestone samples is magnetite, whereas magnetic carriers in the Lower Cretaceous volcaniclastic samples are magnetite and minor amounts of hematite/goethite formed during late-stage weathering.

5. We explore two possible scenarios for the timing of remagnetization. Scenario 1 assumes no rotation of the section relative to India after remagnetization; Scenario 2 assumes no paleolatitudinal motion of the section relative to India after remagnetization. Scenario 1 suggests a 103–83 Ma remagnetization event, whereas Scenario 2 suggests remagnetization at 77–74.3, 73.7–72, or 69–67 Ma. Scenario 1 requires Cretaceous paleolatitudinal growth of Greater India in the Cretaceous, but Scenario 2 requires counterclockwise rotation of the Tibetan Himalaya after remagnetization.

6. During the Early Cretaceous, the region of the Tibetan Himalaya studied here was not separated from India, as far as paleolatitude can be discriminated, confirming previous results of *Klootwijk and Bingham* [1980] from the Thakkhola region to the west. Between the deposition of the volcaniclastic sandstones and remagnetization of the underlying Jurassic limestones, the section underwent a significant clockwise rotation, which we interpret to be associated with well-documented Early Cretaceous extension in the Tibetan Himalaya.

7. The Jurassic limestones may have been remagnetized by a chemical remagnetization associated with postdepositional oxidation of pyrite to magnetite during oxidized fluid circulation. In contrast, the Lower Cretaceous volcaniclastic sandstones mostly retain a primary remanence, probably because the black shales above and below then protected them from fluid circulation.

References

Aben, F. M., M. J. Dekkers, R. R. Bakker, D. J. J. van Hinsbergen, W. J. Zachariasse, G. W. Tate, N. McQuarrie, R. Harris, and B. Duffy (2014), Untangling inconsistent magnetic polarity records through an integrated rock magnetic analysis: A case study on Neogene sections in East Timor, *Geochem. Geophys. Geosyst.*, *15*, 2531–2554, doi:10.1002/2014GC005294.

Abrajevitch, A., and K. Kodama (2009), Biochemical vs. detrital mechanism of remanence acquisition in marine carbonates: A lesson from the K-T boundary interval, *Earth Planet. Sci. Lett.*, *286*(1), 269–277.

Aitchison, J. C., and J. R. Ali (2012), India-Asia collision timing, *Proc. Natl. Acad. Sci. U. S. A.*, *109*(40), E2645, doi:10.1073/pnas.1207859109.

Appel, E., R. Müller, and R. Widder (1991), Paleomagnetic results from the Tibetan Sedimentary Series of the Manang area (north central Nepal), *Geophys. J. Int.*, *104*(2), 255–266.

Appel, E., H. Li, A. Patzelt, and J. Wang (1998), Palaeomagnetic results from late Cretaceous and early Tertiary limestones from Tingri area, southern Tibet, China, *J. Nepal Geol. Soc.*, *18*, 113–124.

Appel, E., C. Crouzet, and E. Schill (2012), Pyrrhotite remagnetizations in the Himalaya: A review, *Geol. Soc. Spec. Publ.*, *371*(1), 163–180.

Belkaaloul, N. K., and D. M. Aïssaoui (1997), Nature and origin of magnetic minerals within the Middle Jurassic shallow-water carbonate rocks of the Paris Basin, France: Implications for magnetostratigraphic dating, *Geophys. J. Int.*, *130*(2), 411–421.

Besse, J., V. Courtillot, J. P. Pozzi, M. Westphal, and Y. X. Zhou (1984), Paleomagnetic estimates of crustal shortening in the Himalayan thrusts and Zangbo suture, *Nature*, *311*, 621–626.

Blumstein, A. M., R. D. Elmore, M. H. Engel, C. Elliot, and A. Basu (2004), Paleomagnetic dating of burial diagenesis in Mississippian carbonates, Utah, *J. Geophys. Res.*, *109*, B04101, doi:10.1029/2003JB002698.

Cairanne, G., C. Aubourg, J.-P. Pozzi, M.-G. Moreau, T. Decamps, and G. Marolleau (2004), Laboratory chemical remanent magnetization in a natural claystone: A record of two magnetic polarities, *Geophys. J. Int.*, *159*(3), 909–916.

Channell, J., and C. McCabe (1994), Comparison of magnetic hysteresis parameters of unremagnetized and remagnetized limestones, *J. Geophys. Res.*, *99*(B3), 4613–4623, doi:10.1029/93JB02578.

Crouzet, C., P. Gautam, E. Schill, and E. Appel (2003), Multicomponent magnetization in western Dolpo (Tethyan Himalaya, Nepal): Tectonic implications, *Tectonophysics*, *377*(1), 179–196.

Crouzet, C., E. Appel, R. El Bay, L. Ding, I. Dunkl, C. Montomoli, R. Carosi, Q. Zhang, and B. Wauschkuhn (2012), Kinematics of the crust around the Ama Drime Massif (southern Tibet)—Constraints from paleomagnetic results, *J. Asian Earth Sci.*, *58*, 119–131.

Day, R., M. Fuller, and V. Schmidt (1977), Hysteresis properties of titanomagnetites: Grain-size and compositional dependence, *Phys. Earth Planet. Inter.*, *13*(4), 260–267.

DeCelles, P., P. Kapp, G. Gehrels, and L. Ding (2014), Paleocene-Eocene foreland basin evolution in the Himalaya of southern Tibet and Nepal: Implications for the age of initial India-Asia collision, *Tectonics*, *33*, 824–849, doi:10.1002/2014TC003522.

Deenen, M. H. L., C. G. Langereis, D. J. J. van Hinsbergen, and A. J. Biggin (2011), Geomagnetic secular variation and the statistics of paleomagnetic directions, *Geophys. J. Int.*, *186*(2), 509–520.

Dekkers, M. J. (2012), End-member modelling as an aid to diagnose remagnetization: A brief review, *Geol. Soc. Spec. Publ.*, *371*(1), 253–269.

Dekkers, M. J., and H. S. Pietersen (1992), Magnetic properties of low-Ca flyash: A rapid tool for Fe-assessment and a proxy for environmental hazard, in *Advanced Cementitious Systems: Mechanisms and Properties, Materials Research Society Symposium Proceedings*, vol. 245, pp. 34–47.

Du, X., X. Chen, C. Wang, Y. Wei, L. Yalin, and L. Jansa (2015), Geochemistry and detrital zircon U–Pb dating of Lower Cretaceous volcaniclastics in the Babazhadong section, Northern Tethyan Himalaya: Implications for the breakup of Eastern Gondwana, *Cretaceous Res.*, *52*, 127–137.

Dunlop, D. J. (2002a), Theory and application of the Day plot (M_{rs}/M_s versus H_{cr}/H_c): 1. Theoretical curves and tests using titanomagnetite data, *J. Geophys. Res.*, *107*(B3), 2056, doi:10.1029/2001JB000486.

Dunlop, D. J. (2002b), Theory and application of the Day plot (M_{rs}/M_s versus H_{cr}/H_c): 2. Application to data for rocks, sediments, and soils, *J. Geophys. Res.*, *107*(B3), 2057, doi:10.1029/2001JB000487.

Dupont-Nivet, G., D. J. J. van Hinsbergen, and T. H. Torsvik (2010a), Persistently low Asian paleolatitudes: Implications for the India-Asia collision history, *Tectonics*, *29*, TC5016, doi:10.1029/2008TC002437.

Dupont-Nivet, G., P. C. Lippert, D. J. J. van Hinsbergen, M. J. M. Meijers, and P. Kapp (2010b), Palaeolatitude and age of the Indo-Asia collision: Palaeomagnetic constraints, *Geophys. J. Int.*, *182*(3), 1189–1198.

Elmore, R. D., J. Kelley, M. Evans, and M. T. Lewchuk (2001), Remagnetization and orogenic fluids: Testing the hypothesis in the central Appalachians, *Geophys. J. Int.*, *144*(3), 568–576.

Elmore, R. D., J. L.-E. Foucher, M. Evans, M. Lewchuk, and E. Cox (2006), Remagnetization of the tonoloway formation and the Helderberg Group in the Central Appalachians: Testing the origin of syntilting magnetizations, *Geophys. J. Int.*, *166*(3), 1062–1076.

Elmore, R. D., A. R. Muxworthy, and M. Aldana (2012), Remagnetization and chemical alteration of sedimentary rocks, *Geol. Soc. Spec. Publ.*, *371*(1), 1–21.

Fabian, K. (2003), Some additional parameters to estimate domain state from isothermal magnetization measurements, *Earth Planet. Sci. Lett.*, *213*(3), 337–345.

Freeman, R. (1986), Magnetic mineralogy of pelagic limestones, *Geophys. J. Int.*, *85*(2), 433–452.

Fruit, D., R. D. Elmore, and S. Halgedahl (1995), Remagnetization of the folded Belden Formation, northwest Colorado, *J. Geophys. Res.*, *100*(B8), 15,009–15,023, doi:10.1029/95JB00045.

Gaetani, M., and E. Garzanti (1991), Multicyclic history of the Northern India continental margin (Northwestern Himalaya)(1), *AAPG Bull.*, *75*(9), 1427–1446.

Gansser, A. (1964), *Geology of the Himalayas*, Interscience, New York.

Garzanti, E., and X. Hu (2014), Latest Cretaceous Himalayan tectonics: Obduction, collison or deccan-related uplift?, *Gondwana Res.*, doi: 10.1016/j.gr.2014.1003.010, in press.

Garzanti, E., R. Haas, and F. Jadoul (1989), Ironstones in the Mesozoic passive margin sequence of the Tethys Himalaya (Zanskar, Northern India): Sedimentology and metamorphism, *Geol. Soc. Spec. Publ.*, *46*, 229–244.

Garzanti, E., M. Gorza, L. Martellini, and A. Nicora (1994), Transition from diagenesis to metamorphism in the Paleozoic to Mesozoic succession of the Dolpo-Manang Synclinorium and Thakkhola Graben (Nepal Tethys Himalaya), *Eclogae Geol. Helv.*, *87*(2), 613–632.

Gong, Z., M. Dekkers, J. Dinarès-Turell, and T. Mullender (2008), Remagnetization mechanism of Lower Cretaceous rocks from the Organya basin (Pyrenees, Spain), *Stud. Geophys. Geod.*, *52*(2), 187–210.

Gong, Z., M. Dekkers, D. Heslop, and T. Mullender (2009), End-member modelling of isothermal remanent magnetization (IRM) acquisition curves: A novel approach to diagnose remagnetization, *Geophys. J. Int.*, *178*(2), 693–701.

Gradstein, F. M., J. G. Ogg, M. Schmitz, and G. Ogg (2012), *The Geologic Time Scale 2012*, Cambridge Univ. Press, Cambridge, U. K.

Harlan, S. S., J. W. Geissman, L. W. Snee, and R. L. Reynolds (1996), Late Cretaceous remagnetization of Proterozoic mafic dikes, southern Highland Mountains, southwestern Montana: A paleomagnetic and ^{40}Ar/^{39}Ar study, *Geol. Soc. Am. Bull.*, *108*(6), 653–668.

Hu, X., L. Jansa, C. Wang, M. Sarti, K. Bak, M. Wagreich, J. Michalik, and J. Soták (2005), Upper Cretaceous oceanic red beds (CORBs) in the Tethys: Occurrences, lithofacies, age, and environments, *Cretaceous Res.*, *26*(1), 3–20.

Hu, X., W. Cheng, and J. Ji (2009), Origin of Cretaceous oceanic red beds from the Vispi Quarry section, central Italy: Visible reflectance and inorganic geochemistry, in *Cretaceous Oceanic Red Beds: Stratigraphy, Composition, Origins and Paleoceanographic and Paleoclimatic Significance, SEPM Spec. Publ.*, vol. 91, pp. 183–197.

Hu, X., L. Jansa, L. Chen, W. L. Griffin, S. Y. O'Reilly, and J. Wang (2010), Provenance of Lower Cretaceous Wölong volcaniclastics in the Tibetan Tethyan Himalaya: Implications for the final breakup of eastern Gondwana, *Sediment. Geol.*, *223*(3), 193–205.

Huang, W., G. Dupont-Nivet, P. C. Lippert, D. J. van Hinsbergen, and E. Hallot (2013), Inclination shallowing in Eocene Linzizong sedimentary rocks from Southern Tibet: Correction, possible causes and implications for reconstructing the India-Asia collision, *Geophys. J. Int.*, *194*(3), 1390–1411.

Jackson, M. (1990), Diagenetic sources of stable remanence in remagnetized Paleozoic cratonic carbonates: A rock magnetic study, *J. Geophys. Res.*, *95*(B3), 2753–2761, doi:10.1029/JB095iB03p02753.

Jackson, M., and N. L. Swanson-Hysell (2012), Rock magnetism of remagnetized carbonate rocks: Another look, *Geol. Soc. Spec. Publ.*, *371*(1), 229–251.

Jackson, M., C. McCabe, M. M. Ballard, and R. Van der Voo (1988), Magnetite authigenesis and diagenetic paleotemperatures across the northern Appalachian basin, *Geology*, *16*(7), 592–595.

Jadoul, F., F. Berra, and E. Garzanti (1998), The Tethys Himalayan passive margin from Late Triassic to Early Cretaceous (South Tibet), *J. Asian Earth Sci.*, *16*(2), 173–194.

Jenkyns, H. (1980), Cretaceous anoxic events: From continents to oceans, *J. Geol. Soc. London*, *137*(2), 171–188.

Karlin, R., and S. Levi (1983), Diagenesis of magnetic minerals in recent haemipelagic sediments, *Nature*, *303*(5915), 327–330.

Katz, B., R. D. Elmore, M. Cogoini, M. H. Engel, and S. Ferry (2000), Associations between burial diagenesis of smectite, chemical remagnetization, and magnetite authigenesis in the Vocontian trough, SE France, *J. Geophys. Res.*, *105*(B1), 851–868, doi:10.1029/1999JB900309.

Kent, D. V. (1985), Thermoviscous remagnetization in some Appalachian limestones, *Geophys. Res. Lett.*, *12*(12), 805–808, doi:10.1029/GL012i012p00805.

Kirschvink, J. (1980), The least-squares line and plane and the analysis of palaeomagnetic data, *Geophys. J. Int.*, *62*(3), 699–718.

Klootwijk, C. T., and D. K. Bingham (1980), The extent of Greater India, III. Paleomagnetic data from the Tibetan Sedimentary series, Thakkhola region, Nepal Himalaya, *Earth Planet. Sci. Lett.*, *51*(2), 381–405.

Klootwijk, C. T., S. Shah, J. Gergan, M. L. Sharma, B. Tirkey, and B. Gupta (1983), A paleomagnetic reconnaissance of Kashmir, northwestern Himalaya, India, *Earth Planet. Sci. Lett.*, *63*(2), 305–324.

Kopp, R. E., and J. L. Kirschvink (2008), The identification and biogeochemical interpretation of fossil magnetotactic bacteria, *Earth Sci. Rev.*, *86*(1), 42–61.

Kruiver, P. P., M. J. Dekkers, and D. Heslop (2001), Quantification of magnetic coercivity components by the analysis of acquisition curves of isothermal remanent magnetisation, *Earth Planet. Sci. Lett.*, *189*(3), 269–276.

Lanci, L., and D. V. Kent (2006), Meteoric smoke fallout revealed by superparamagnetism in Greenland ice, *Geophys. Res. Lett.*, *33*, L13308, doi:10.1029/2006GL026480.

Lanci, L., D. V. Kent, and P. E. Biscaye (2007), Meteoric smoke concentration in the Vostok ice core estimated from superparamagnetic relaxation and some consequences for estimates of Earth accretion rate, *Geophys. Res. Lett.*, *34*, L10803, doi:10.1029/2007GL029811.

Lanci, L., B. Delmonte, V. Maggi, J.-R. Petit, and D. V. Kent (2008), Ice magnetization in the EPICA-Dome C ice core: Implication for dust sources during glacial and interglacial periods, *J. Geophys. Res.*, *113*, D14207, doi:10.1029/2007JD009678.

Leckie, R. M., T. J. Bralower, and R. Cashman (2002), Oceanic anoxic events and plankton evolution: Biotic response to tectonic forcing during the mid-Cretaceous, *Paleoceanography*, *17*(3), doi:10.1029/2001PA000623.

Liebke, U., E. Appel, L. Ding, and Q. Zhang (2013), Age constraints on the India-Asia collision derived from secondary remanences of Tethyan Himalayan sediments from the Tingri area, *J. Asian Earth Sci.*, *62*, 329–340.

Lippert, P. C., D. J. J. van Hinsbergen, and G. Dupont-Nivet (2014), The Early Cretaceous to present latitude of the central Lhasa-plano (Tibet): A paleomagnetic synthesis with implications for Cenozoic tectonics, paleogeography and climate of Asia, in *Towards an Improved Understanding of Uplift Mechanisms and the Elevation History of the Tibetan Plateau, Geol. Soc. Am. Spec. Pap. 507*, edited by J. S. Nie, G. D. Hoke, and B. K. Horton, pp. 1–21, Geol. Soc. Am.

Lovley, D. R., J. F. Stolz, G. L. Nord, and E. J. Phillips (1987), Anaerobic production of magnetite by a dissimilatory iron-reducing microorganism, *Nature*, *330*(6145), 252–254.

Lowrie, W. (1990), Identification of ferromagnetic minerals in a rock by coercivity and unblocking temperature properties, *Geophys. Res. Lett.*, *17*(2), 159–162, doi:10.1029/GL017i002p00159.

McCabe, C., and J. Channell (1994), Late Paleozoic remagnetization in limestones of the Craven Basin (northern England) and the rock magnetic fingerprint of remagnetized sedimentary carbonates, *J. Geophys. Res.*, *99*(B3), 4603–4612, doi:10.1029/93JB02802.

McCabe, C., R. Van der Voo, D. R. Peacor, C. R. Scotese, and R. Freeman (1983), Diagenetic magnetite carries ancient yet secondary remanence in some Paleozoic sedimentary carbonates, *Geology*, *11*(4), 221–223.

McCabe, C., M. Jackson, and B. Saffer (1989), Regional patterns of magnetite authigenesis in the Appalachian Basin: Implications for the mechanism of Late Paleozoic remagnetization, *J. Geophys. Res.*, *94*(B8), 10,429–10,443, doi:10.1029/JB094iB08p10429.

McFadden, P. L., and F. J. Lowes (1981), The discrimination of mean directions drawn from Fisher distributions, *Geophys. J. R. Astron. Soc.*, *67*, 19–33.

McFadden, P. L., and M. W. McElhinny (1988), The combined analysis of remagnetization circles and direct observations in palaeomagnetism, *Earth Planet. Sci. Lett.*, *87*(1–2), 161–172.

Meijers, M. J. M., D. J. J. van Hinsbergen, M. J. Dekkers, D. Altıner, N. Kaymakcı, and C. G. Langereis (2011), Pervasive Paleogene remagnetization of the central Taurides fold-and-thrust belt (southern Turkey) and implications for rotations in the Isparta Angle, *Geophys. J. Int.*, *184*(3), 1090–1112.

Ménabréaz, L., N. Thouveny, G. Camoin, and S. P. Lund (2010), Paleomagnetic record of the late Pleistocene reef sequence of Tahiti (French Polynesia): A contribution to the chronology of the deposits, *Earth Planet. Sci. Lett.*, *294*(1), 58–68.

Moskowitz, B. M., D. A. Bazylinski, R. Egli, R. B. Frankel, and K. J. Edwards (2008), Magnetic properties of marine magnetotactic bacteria in a seasonally stratified coastal pond (Salt Pond, MA, USA), *Geophys. J. Int.*, *174*(1), 75–92.

Mullender, T. A. T., T. Frederichs, C. Hilgenfeldt, K. Fabian, and M. J. Dekkers (2005), Fully automated demagnetization and measurement of NRM, ARM and IRM on a '2G' SQUID magnetometer, Abstract IAGA2005-A-00898 presented at IAGA Conference, Toulouse, France.

Muttoni, G. (1995), ''Wasp-waisted'' hysteresis loops from a pyrrhotite and magnetite-bearing remagnetized Triassic limestone, *Geophys. Res. Lett.*, *22*(23), 3167–3170, doi:10.1029/95GL03073.

Neuhuber, S., M. Wagreich, I. Wendler, and C. Spötl (2007), Turonian Oceanic Red Beds in the Eastern Alps: Concepts for palaeoceanographic changes in the Mediterranean Tethys, *Palaeogeogr. Palaeoclimatol. Palaeoecol.*, *251*(2), 222–238.

Oliva-Urcia, B., E. L. Pueyo, and J. C. Larrasoaña (2008), Magnetic reorientation induced by pressure solution: A potential mechanism for orogenic-scale remagnetizations, *Earth Planet. Sci. Lett.*, *265*(3), 525–534.

Patzelt, A., H. Li, J. Wang, and E. Appel (1996), Palaeomagnetism of Cretaceous to Tertiary sediments from southern Tibet: Evidence for the extent of the northern margin of India prior to the collision with Eurasia, *Tectonophysics*, *259*, 259–284.

Pike, C. R., A. P. Roberts, and K. L. Verosub (1999), Characterizing interactions in fine magnetic particle systems using first order reversal curves, *J. Appl. Phys.*, *85*(9), 6660–6667.

Ran, B., C. Wang, X. Zhao, Y. Li, J. Meng, K. Cao, and P. Wang (2012), Dimension of Greater India in the early Mesozoic: Paleomagnetic constraints from Triassic sediments in the Tethyan Himalaya, *J. Asian Earth Sci.*, *53*, 15–24.

Roberts, A. P., and R. Weaver (2005), Multiple mechanisms of remagnetization involving sedimentary greigite (Fe_3S_4), *Earth Planet. Sci. Lett.*, *231*(3), 263–277.

Roberts, A. P., Y. Cui, and K. L. Verosub (1995), Wasp-waisted hysteresis loops: Mineral magnetic characteristics and discrimination of components in mixed magnetic systems, *J. Geophys. Res.*, *100*(B9), 17,909–17,924, doi:10.1029/95JB00672.

Roberts, A. P., C. R. Pike, and K. L. Verosub (2000), First-order reversal curve diagrams: A new tool for characterizing the magnetic properties of natural samples, *J. Geophys. Res.*, *105*(28), 28,461–28,475, doi:10.1029/2000JB900326.

Roberts, A. P., L. Chang, C. J. Rowan, C. S. Horng, and F. Florindo (2011), Magnetic properties of sedimentary greigite (Fe_3S_4): An update, *Rev. Geophys.*, *49*, RG1002, doi:10.1029/2010RG000336.

Roberts, A. P., F. Florindo, L. Chang, D. Heslop, L. Jovane, and J. C. Larrasoaña (2013), Magnetic properties of pelagic marine carbonates, *Earth Sci. Rev.*, *127*, 111–139.

Rowan, C. J., and A. P. Roberts (2005), Tectonic and geochronological implications of variably timed magnetizations carried by authigenic greigite in marine sediments from New Zealand, *Geology*, *33*(7), 553–556.

Rowan, C. J., and A. P. Roberts (2006), Magnetite dissolution, diachronous greigite formation, and secondary magnetizations from pyrite oxidation: Unravelling complex magnetizations in Neogene marine sediments from New Zealand, *Earth Planet. Sci. Lett.*, *241*(1), 119–137.

Schill, E., E. Appel, P. Gautam, and P. Dietrich (2002), Thermo-tectonic history of the Tethyan Himalayas deduced from the palaeomagnetic record of metacarbonates from Shiar Khola (Central Nepal), *J. Asian Earth Sci.*, *20*(3), 203–210.

Schlanger, S., and H. Jenkyns (1976), Cretaceous oceanic anoxic events: Causes and consequences, *Geol. Mijnbouw*, *55*(3–4), 179–184.

Sciunnach, D., and E. Garzanti (2012), Subsidence history of the Tethys Himalaya, *Earth Sci. Rev.*, *111*(1), 179–198.

Smirnov, A. V., and J. A. Tarduno (2001), Estimating superparamagnetism in marine sediments with the time dependency of coercivity of remanence, *J. Geophys. Res.*, *106*(B8), 16,135–16,143, doi:10.1029/2001JB000152.

Suk, D., and S. L. Halgedahl (1996), Hysteresis properties of magnetic spherules and whole rock specimens from some Paleozoic platform carbonate rocks, *J. Geophys. Res.*, *101*(B11), 25,053–25,075, doi:10.1029/96JB02271.

Suk, D., D. Peacor, and R. Van der Voo (1990a), Replacement of pyrite framboids by magnetite in limestone and implications for palaeomagnetism, *Nature*, *345*(6276), 611–613.

Suk, D., R. Van der Voo, and D. R. Peacor (1990b), Scanning and transmission electron microscope observations of magnetite and other iron phases in Ordovician carbonates from east Tennessee, *J. Geophys. Res.*, *95*(B8), 12,327–12,336, doi:10.1029/JB095iB08p12327.

Suk, D., R. Van der Voo, and D. R. Peacor (1991), SEM/STEM observations of magnetite in carbonates of eastern North America: Evidence for chemical remagnettzation during the Alleghenian Orogeny, *Geophys. Res. Lett.*, *18*(5), 939–942, doi:10.1029/91GL00916.

Suk, D., R. Van Der Voo, and D. R. Peacor (1993), Origin of magnetite responsible for remagnetization of early Paleozoic limestones of New York State, *J. Geophys. Res.*, *98*(B1), 419–434, doi:10.1029/92JB01323.

Tarduno, J. A. (1995), Superparamagnetism and reduction diagenesis in pelagic sediments: Enhancement or depletion?, *Geophys. Res. Lett.*, *22*(11), 1337–1340, doi:10.1029/95GL00888.

Tarduno, J. A., and M. Myers (1994), A primary magnetization fingerprint from the Cretaceous Laytonville Limestone: Further evidence for rapid oceanic plate velocities, *J. Geophys. Res.*, *99*(B11), 21,691–21,703, doi:10.1029/94JB01939.

Tauxe, L. (2005), Inclination flattening and the geocentric axial dipole hypothesis, *Earth Planet. Sci. Lett.*, *233*(3–4), 247–261.

Tauxe, L., and D. V. Kent (2004), A simplified statistical model for the geomagnetic field and the detection of shallow bias in paleomagnetic inclinations: Was the ancient magnetic field dipolar?, in *Timescales of the Paleomagnetic Field*, vol. 145, pp. 101–115.

Tauxe, L., and G. Watson (1994), The fold test: An eigen analysis approach, *Earth Planet. Sci. Lett.*, *122*(3), 331–341.

Tauxe, L., T. Mullender, and T. Pick (1996), Potbellies, wasp-waists, and superparamagnetism in magnetic hysteresis, *J. Geophys. Res.*, *101*(B1), 571–583, doi:10.1029/95JB03041.

Tohver, E., A. Weil, J. Solum, and C. Hall (2008), Direct dating of carbonate remagnetization by $^{40}Ar/^{39}Ar$ analysis of the smectite-illite transformation, *Earth Planet. Sci. Lett.*, *274*(3), 524–530.

Torsvik, T. H., R. Van der Voo, U. Preeden, C. Mac Niocaill, B. Steinberger, P. V. Doubrovine, D. J. J. van Hinsbergen, M. Domeier, C. Gaina, and E. Tohver (2012), Phanerozoic polar wander, palaeogeography and dynamics, *Earth Sci. Rev.*, *114*(3), 325–368.

Turgeon, S. C., and R. A. Creaser (2008), Cretaceous oceanic anoxic event 2 triggered by a massive magmatic episode, *Nature*, *454*(7202), 323–326.

Van Hinsbergen, D. J. J., M. J. Dekkers, and A. Koc (2010), Testing Miocene remagnetization of Bey Dağları: Timing and amount of Neogene rotations in SW Turkey, *Turk. J. Earth Sci.*, *19*, 123–156.

van Hinsbergen, D. J. J., P. C. Lippert, G. Dupont-Nivet, N. McQuarrie, P. V. Doubrovine, W. Spakman, and T. H. Torsvik (2012), Greater India Basin hypothesis and a two-stage Cenozoic collision between India and Asia, *Proc. Natl. Acad. Sci. U. S. A.*, *109*(20), 7659–7664.

Wang, C., X. Hu, M. Sarti, R. W. Scott, and X. Li (2005), Upper Cretaceous oceanic red beds in southern Tibet: A major change from anoxic to oxic, deep-sea environments, *Cretaceous Res.*, *26*(1), 21–32.

Wang, C., J. Dai, X. Zhao, Y. Li, S. A. Graham, D. He, B. Ran, and J. Meng (2014), Outward-growth of the Tibetan Plateau during the Cenozoic: A review, *Tectonophysics*, *621*, 1–43.

Weil, A. B., and R. Van der Voo (2002), Insights into the mechanism for orogen-related carbonate remagnetization from growth of authigenic Fe-oxide: A scanning electron microscopy and rock magnetic study of Devonian carbonates from northern Spain, *J. Geophys. Res.*, *107*(B4), doi:10.1029/2001JB000200.

Wilkin, R., H. Barnes, and S. Brantley (1996), The size distribution of framboidal pyrite in modern sediments: An indicator of redox conditions, *Geochim. Cosmochim. Acta*, *60*(20), 3897–3912.

Woods, S. D., R. Elmore, and M. Engel (2002), Paleomagnetic dating of the smectite to illite conversion: Testing the hypothesis in Jurassic sedimentary rocks, Skye, Scotland, *J. Geophys. Res.*, *107*(B5), 2091, doi:10.1029/2000JB000053.

Xu, W., R. Van der Voo, and D. R. Peacor (1998), Electron microscopic and rock magnetic study of remagnetized Leadville carbonates, central Colorado, *Tectonophysics*, *296*(3), 333–362.

Yi, Z., B. Huang, J. Chen, L. Chen, and H. Wang (2011), Paleomagnetism of early Paleogene marine sediments in southern Tibet, China: Implications to onset of the India-Asia collision and size of Greater India, *Earth Planet. Sci. Lett.*, *309*(1), 153–165.

Zegers, T., M. Dekkers, and S. Bailly (2003), Late Carboniferous to Permian remagnetization of Devonian limestones in the Ardennes: Role of temperature, fluids, and deformation, *J. Geophys. Res.*, *108*(B7), 2357, doi:10.1029/2002JB002213.